cmgh
CELLULAR AND MOLECULAR GASTROENTEROLOGY AND HEPATOLOGY

ORIGINAL RESEARCH

Endothelin Receptor-A Inhibition Decreases Ductular Reaction, Liver Fibrosis, and Angiogenesis in a Model of Cholangitis

Travis Owen,[1] Guido Carpino,[2] Lixian Chen,[1] Debjyoti Kundu,[1] Payton Wills,[1] Burcin Ekser,[3] Paolo Onori,[2] Eugenio Gaudio,[2] Gianfranco Alpini,[1,4] Heather Francis,[1,4] and Lindsey Kennedy[1,4]

[1]Division of Gastroenterology and Hepatology, Department of Medicine, Indiana University School of Medicine, Indianapolis, Indiana; [2]Department of Anatomical, Histological, Forensic Medicine and Orthopedics Sciences, Sapienza University of Rome, Rome, Italy; [3]Division of Transplant Surgery, Department of Surgery, Indiana University School of Medicine, Indianapolis, Indiana; and [4]Department of Research, Richard L. Roudebush VA Medical Center, Indianapolis, Indiana

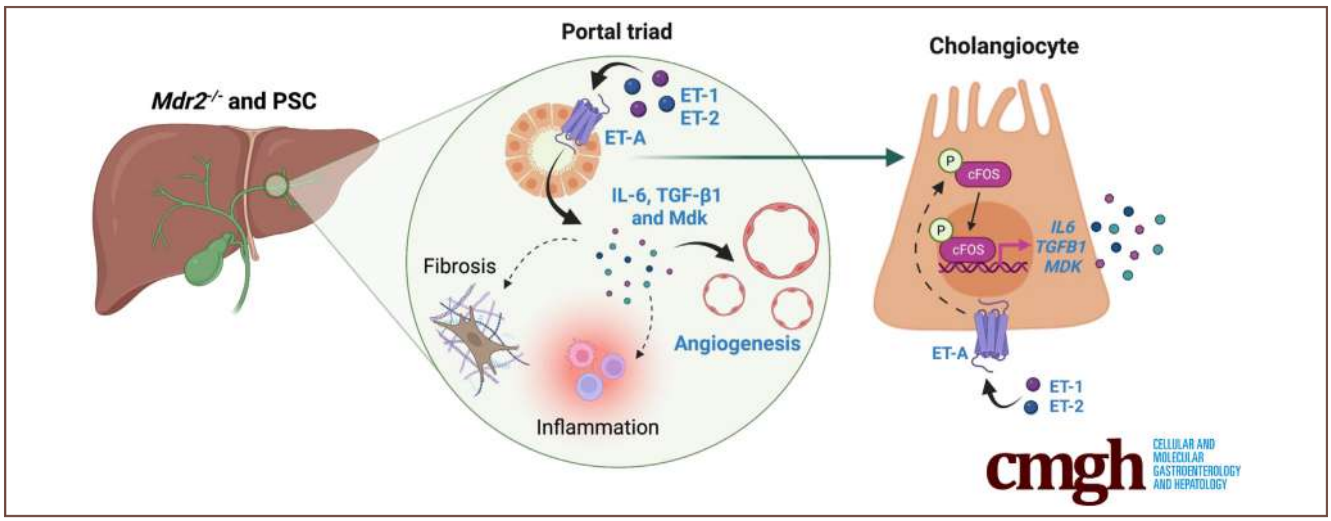

SUMMARY

Primary sclerosing cholangitis (PSC) and a PSC mouse model have enhanced endothelin (ET)-1, ET-2, and ET-A expression. ET-A inhibition reduced ductular reaction, inflammation, fibrosis, and angiogenesis in the PSC model. ET-A regulated biliary angiocrine signaling that may influence endothelial cells.

BACKGROUND & AIMS: Primary sclerosing cholangitis (PSC) leads to ductular reaction and fibrosis and is complicated by vascular dysfunction. Cholangiocyte and endothelial cell crosstalk modulates their proliferation in cholestatic models. Endothelin (ET)-1 and ET-2 bind to their receptor, ET-A, and cholangiocytes are a key source of ET-1 after bile duct ligation. We aimed to evaluate the therapeutic potential of ET-A inhibition in PSC and biliary-endothelial crosstalk mediated by this pathway.

METHODS: Wild-type and multidrug resistance 2 knockout (*Mdr2*$^{-/-}$) mice at 12 weeks of age were treated with vehicle or Ambrisentan (ET-A antagonist) for 1 week by daily intraperitoneal injections. Human control and PSC samples were used.

RESULTS: *Mdr2*$^{-/-}$ mice at 4, 8, and 12 weeks displayed angiogenesis that peaked at 12 weeks. *Mdr2*$^{-/-}$ mice at 12 weeks had enhanced biliary ET-1/ET-2/ET-A expression and secretion, whereas human PSC had enhanced ET-1/ET-A expression and secretion. Ambrisentan reduced biliary damage, immune cell infiltration, and fibrosis in *Mdr2*$^{-/-}$ mice. *Mdr2*$^{-/-}$ mice had squamous cholangiocytes with blunted microvilli and dilated arterioles lacking cilia; however, Ambrisentan reversed these alterations. Ambrisentan decreased cholangiocyte expression of pro-angiogenic factors, specifically midkine, through the regulation of cFOS. *In vitro*, ET-1/ET-A caused cholangiocyte senescence, endothelial cell angiogenesis, and macrophage inflammation. *In vitro*, human PSC cholangiocyte supernatants increased endothelial cell migration, which was blocked with Ambrisentan treatment.

CONCLUSIONS: ET-A inhibition reduced biliary and liver damage in *Mdr2*$^{-/-}$ mice. ET-A promotes biliary angiocrine signaling that may, in turn, enhance angiogenesis. Targeting ET-A may prove therapeutic for PSC, specifically patients displaying vascular dysfunction. *(Cell Mol Gastroenterol Hepatol 2023;16:513–540; https://doi.org/10.1016/j.jcmgh.2023.06.005)*

Keywords: Midkine; Endothelial Cells; Liver Fibrosis; Cholangiopathies.

See editorial on page 643.

Primary sclerosing cholangitis (PSC) is a cholestatic disease that targets cholangiocytes leading to biliary senescence, inflammation, fibrosis and ultimately cirrhosis.[1] Bile duct damage leads to cholangiocyte senescence and ductular reaction, which contribute to hepatic changes through paracrine signaling.[2] Biliary-derived factors promote immune cell infiltration and hepatic stellate cell (HSC) activation,[2] and the interplay between reactive ductular cells and endothelial cells is undefined. Understanding components that mediate angiogenesis is critical because vascular dysfunction and angiogenic signaling are dynamic contributors to portal hypertension in cholestatic diseases.[3]

In cholestatic models, ductular reaction contributes to vascular remodeling via angiocrine signaling. Specifically, in models of cholestasis ductular reaction is coupled with an increase in neovessel presence and angiogenesis.[4] This process was mediated by the angiocrine signal, Slit2, released specifically by cholangiocytes.[4] In humans undergoing liver transplantation, ischemic injury causes peribiliary vascular plexus (PVP) (blood supply of the bile ducts) loss and reduces biliary proliferation.[5] Endothelial cell presence is enhanced in multidrug resistance 2 knockout (*Mdr2*$^{-/-}$) mice and human PSC samples.[6,7] Arterial luminal dilation and portal angiogenesis occur in idiopathic portal hypertension.[8] More work is necessary to understand which biliary-derived components drive angiogenesis.

Endothelin (ET) includes a set of peptides, ET-1, ET-2 and ET-3, that bind to and activate their specific G-protein coupled receptors, ET-A (binding affinity ET-1 = ET-2 > ET-3) and ET-B (binding affinity ET-1 = ET-2 = ET-3).[9] ETs are vasoactive peptides, but ET-A induces vasoconstriction, growth, and inflammation, whereas ET-B promotes vasodilation and inhibits growth and inflammation in cardiovascular disease.[10] ET-A inhibition reduces liver fibrosis in bile duct ligated (BDL) rats,[11] whereas inhibition of ET-B is associated with increased portal pressure in normal mice and sinusoidal constriction during cirrhosis.[12] ET-1 administration prolongs bile retention[13] and induces cholestasis and vasoconstriction in isolated perfused rat livers[14]; however, ET signaling in PSC is unknown. Therefore, we aimed to determine how cholangiocytes influence angiogenesis during cholestasis specifically through ET-A signaling.

Results

Aging Mdr2$^{-/-}$ *Mice and Human PSC Samples Present With Angiogenesis*

Progressive liver damage occurs during aging in *Mdr2*$^{-/-}$ mice, with ductular reaction occurring at 3 weeks of age[15]; however, information on angiogenesis is lacking. Angiogenesis increased in *Mdr2*$^{-/-}$ mice at 8 weeks and 12 weeks of age, with vessel presence (red arrowheads) peaking at 12 weeks (Figure 1*A*). Similar staining pattern was found for von Willebrand factor (vWF) (Figure 1*B*). Parallel to *Mdr2*$^{-/-}$ mice, we found enhanced angiogenesis in human PSC (Figure 1*C* and *D*).

ET-1, ET-2, and ET-A Expression and Secretion Increase in Mdr2$^{-/-}$ *Mice and Human PSC*

Because angiogenesis was highest in *Mdr2*$^{-/-}$ mice at 12 weeks, we used this age for our studies. Biliary immunoreactivity of ET-1, ET-2, and ET-A increased in *Mdr2*$^{-/-}$ mice compared with wild-type (WT) (Figure 2*A*). ET-1, ET-2, and ET-A immunoreactivity in endothelial cells (pink) and cholangiocytes (red) increased in *Mdr2*$^{-/-}$ mice compared with WT (Figure 3*A*). The secretion of ET-1 and ET-2 was enhanced in cholangiocyte supernatants from *Mdr2*$^{-/-}$ mice compared with WT (Figure 2*B*).

PSC patients had increased immunoreactivity of ET-1, ET-2, and ET-A in cholangiocytes and endothelial cells (Figure 2*C*, Figure 3*B*); however, mRNA expression of *EDN1* and *EDNRA* increased in cholangiocytes from PSC patients with no significant change in *EDN2* compared with controls (Figure 2*D*). ET-1, but not ET-2, levels in bile and cholangiocyte supernatants increased in human PSC compared with control (Figure 2*E* and *F*). It is important to note that there may be discrepancies in *EDN1*, *EDN2,* and *EDNRA* expression, as well as ET-1 and ET-2 secretion, in the intrahepatic (IH) versus extrahepatic (EH) cholangiocytes (Figure 2*D*); however, because of the limited number of patient-derived cholangiocytes available we were unable to analyze heterogeneity and instead looked at overall changes.

Portal Damage Is Reduced in Ambrisentan-Treated Mdr2$^{-/-}$ *Mice*

The ET-1/ET-2/ET-A axis is enhanced in *Mdr2*$^{-/-}$ mice and human PSC; therefore, we treated WT and *Mdr2*$^{-/-}$ mice at 12 weeks of age with an ET-A antagonist, Ambrisentan, for 1 week. By H&E, we observed increased periductal inflammation, lobular inflammation, necrosis, and portal damage in *Mdr2*$^{-/-}$ mice compared with WT; however, Ambrisentan reduced periductal inflammation and portal damage in *Mdr2*$^{-/-}$ mice (Figure 4*A*). No changes in lobular

Abbreviations used in this paper: **Angpt, angiopoietin; BDL, bile duct ligation; Ccl, C-C motif chemokine ligand; cFOS, Fos proto-oncogene; CK-19, cytokeratin-19; Col1a1, collagen, type I, α 1; DMSO, dimethyl sulfoxide; EH, extrahepatic; ET, endothelin; FFPE, formalin-fixed, paraffin-embedded; hHEP, human hepatocytes; hHSC, human hepatic stellate cell; HIBEC, human intrahepatic biliary epithelial cell; HSC, hepatic stellate cell; HUVEC, human umbilical vein endothelial cells; IH, intrahepatic; IL, interleukin; IPA, Ingenuity Pathway Analysis; Mdk, midkine; *Mdr2*$^{-/-}$, multidrug resistance 2 knockout; OCT, optical cutting temperature; p-cFOS, phospho-Fos proto-oncogene; PlGF, placental growth factor; PSC, primary sclerosing cholangitis; PVP, peribiliary vascular plexus; *q*PCR, quantitative polymerase chain reaction; RE, random expectation; SA-β-Gal, senescence-associated β galactosidase; TEM, transmission electron microscopy; TGF-β1, transforming growth factor-β1; VEGF-A, vascular endothelial growth factor-A; vWF, von Willebrand factor; WT, wild-type.**

Most current article

2352-345X
https://doi.org/10.1016/j.jcmgh.2023.06.005

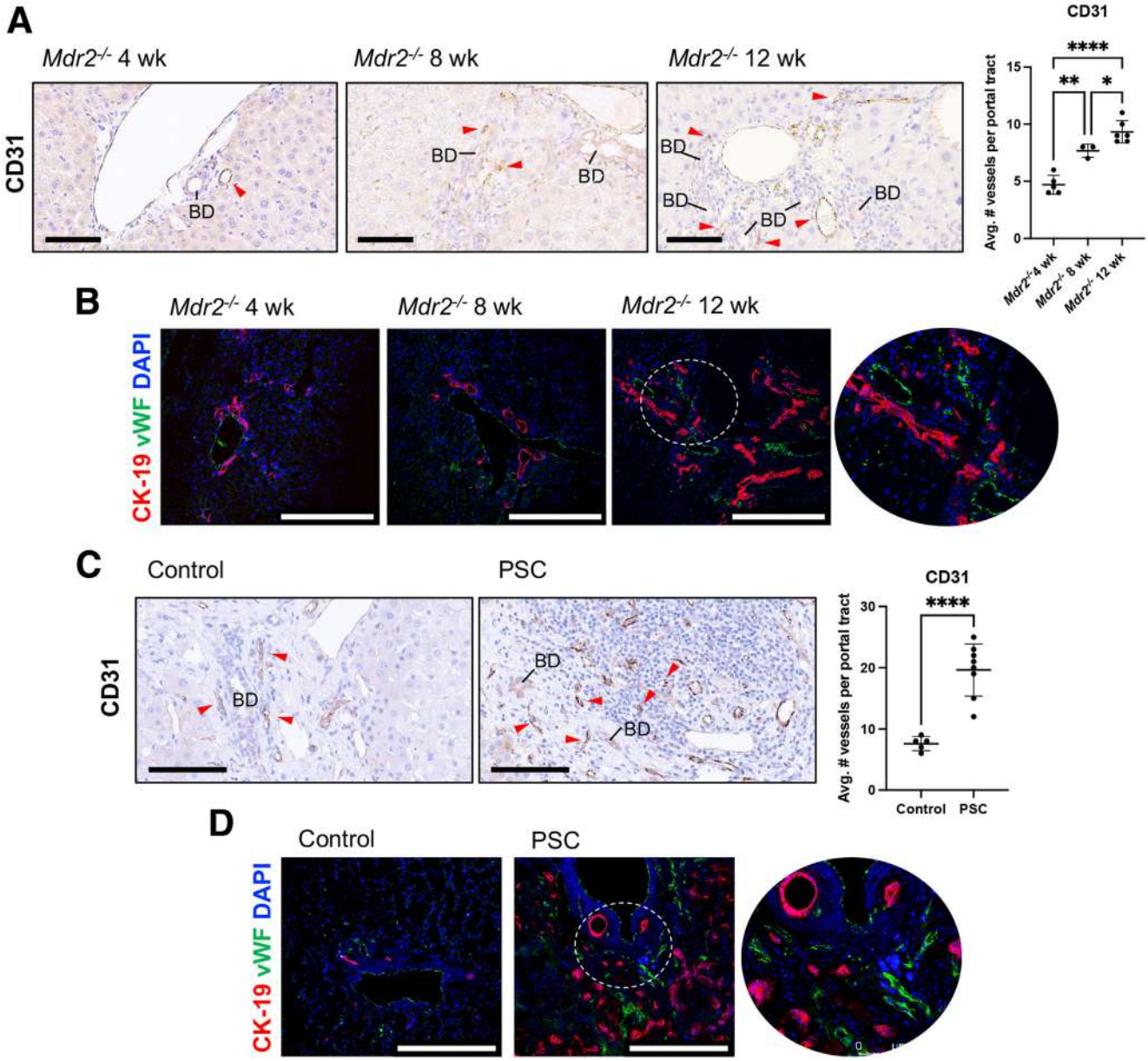

Figure 1. Angiogenesis in aging *Mdr2*$^{-/-}$ mice and human PSC. (*A*) CD31 staining and semiquantification in *Mdr2*$^{-/-}$ mice. (*B*) Co-stain for CK-19 and vWF in *Mdr2*$^{-/-}$ mice. (*C*) CD31 staining and semiquantification in human samples. (*D*) Co-stain for CK-19 and vWF in human samples. Data are mean ± standard deviation. n = 10 portal images per sample imaged from n = 3–6 mice, n = 5 human control, and n = 8 human PSC for CD31. BD, bile duct; *red arrowheads*, vessels. vWF/CK-19 is 20× and 40×, scale bar = 250 μm. CD31 is 40×, scale bar = 200 μm. **P* < .05, ***P* < .01, ****P* < .001, *****P* < .0001.

inflammation or necrosis were noted in Ambrisentan-treated *Mdr2*$^{-/-}$ mice (Figure 4*A*). We found no significant alterations of the heart in any groups (Figure 4*B*). *Mdr2*$^{-/-}$ mice presented with tubular dilation of the kidney, which was unaffected by Ambrisentan (Figure 4*C*). *Mdr2*$^{-/-}$ mice presented with foci of peribronchial inflammation and alveolar hemorrhage, which were reduced with Ambrisentan treatment (Figure 4*D*). No significant alterations were found in treated WT mice versus controls or dimethyl sulfoxide (DMSO)-treated *Mdr2*$^{-/-}$ mice for any organ (Figure 4*A*–*D*).

Ductular Reaction and Biliary Senescence Are Decreased in Ambrisentan-Treated Mdr2$^{-/-}$ *Mice*

Ductular reaction increased in *Mdr2*$^{-/-}$ mice compared with WT; however, Ambrisentan treatment decreased ductular reaction in *Mdr2*$^{-/-}$ mice (Figure 5*A*). Biliary senescence increased in *Mdr2*$^{-/-}$ mice compared with WT but was reduced in Ambrisentan-treated *Mdr2*$^{-/-}$ mice (Figure 5*B* and *C*). Similarly, biliary mRNA expression of *Cdkn1a* was enhanced in *Mdr2*$^{-/-}$ mice compared with WT but was reduced in Ambrisentan-treated *Mdr2*$^{-/-}$ mice (Figure 5*D*). No changes in ductular reaction or

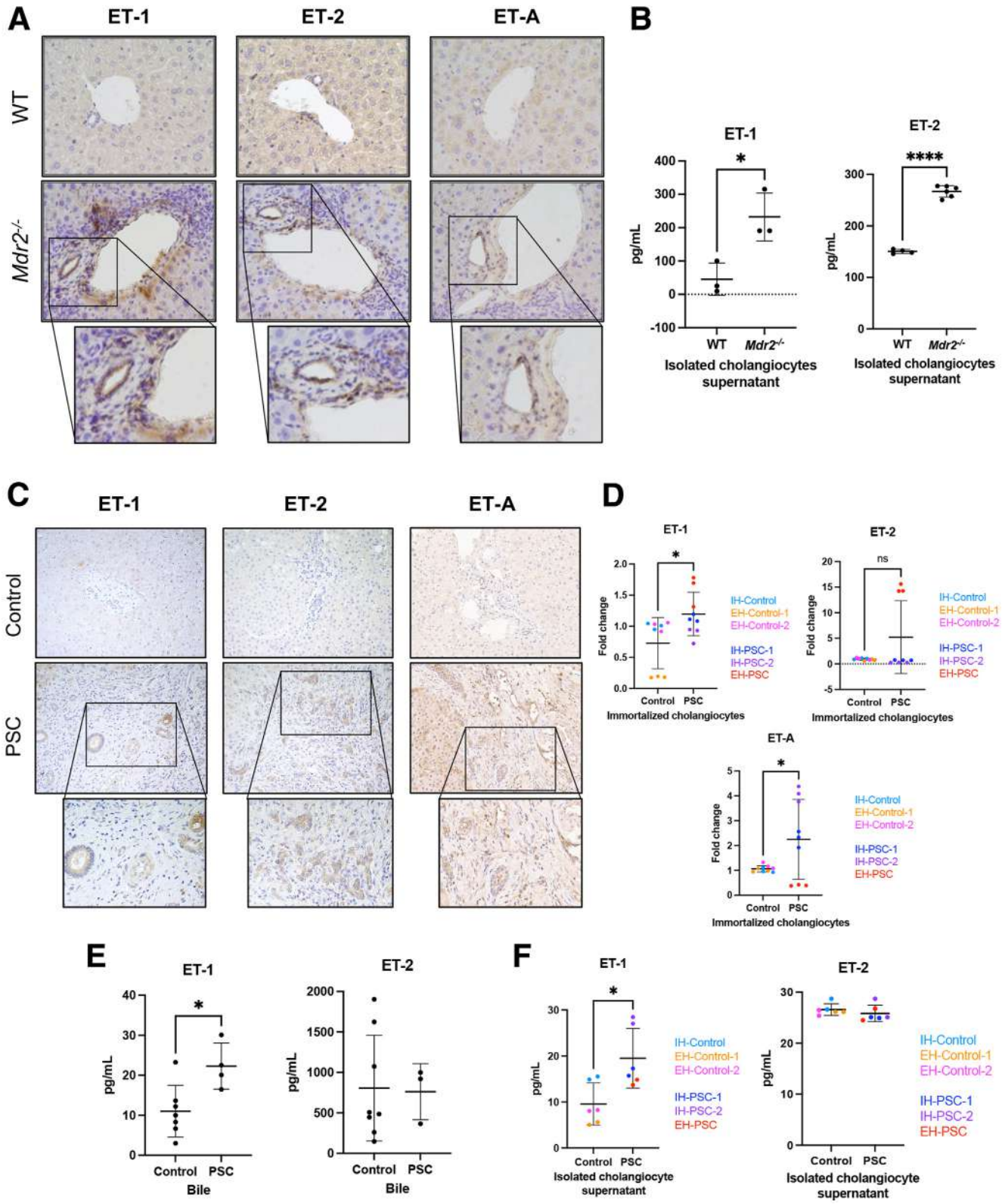

Figure 2. ET-1 and ET-2 expression and secretion and ET-A expression. (*A*) Staining for ET-1, ET2, and ET-A in mouse samples. (*B*) ET-1 and ET-2 levels in cholangiocyte supernatants from mouse samples. (*C*) Staining for ET-1, ET2, and ET-A in human samples. (*D*) *EDN1*, *EDN2*, and *EDNRA* mRNA expression in isolated cholangiocytes from human samples. (*E*) ET-1 and ET-2 levels in bile from human samples. (*F*) ET-1 and ET-2 levels in cholangiocyte supernatants from isolated human cholangiocyte cultures. Data are mean ± standard deviation. n = 3 reactions per sample for *q*PCR in n = 3 control and n = 3 PSC cholangiocyte samples; n = 3 reactions for EIA from cholangiocyte supernatants obtained from n = 8 mice per group; n = 2 reactions per sample for EIA from n = 7–8 control and n = 3–4 PSC bile samples; n = 2 reactions per sample for EIA in cholangiocyte medium from n = 3 control and n = 3 PSC samples. Staining is 20× and 40×, scale bar = 300 μm. *$P < .05$, **$P < .01$, ***$P < .001$, ****$P < .0001$.

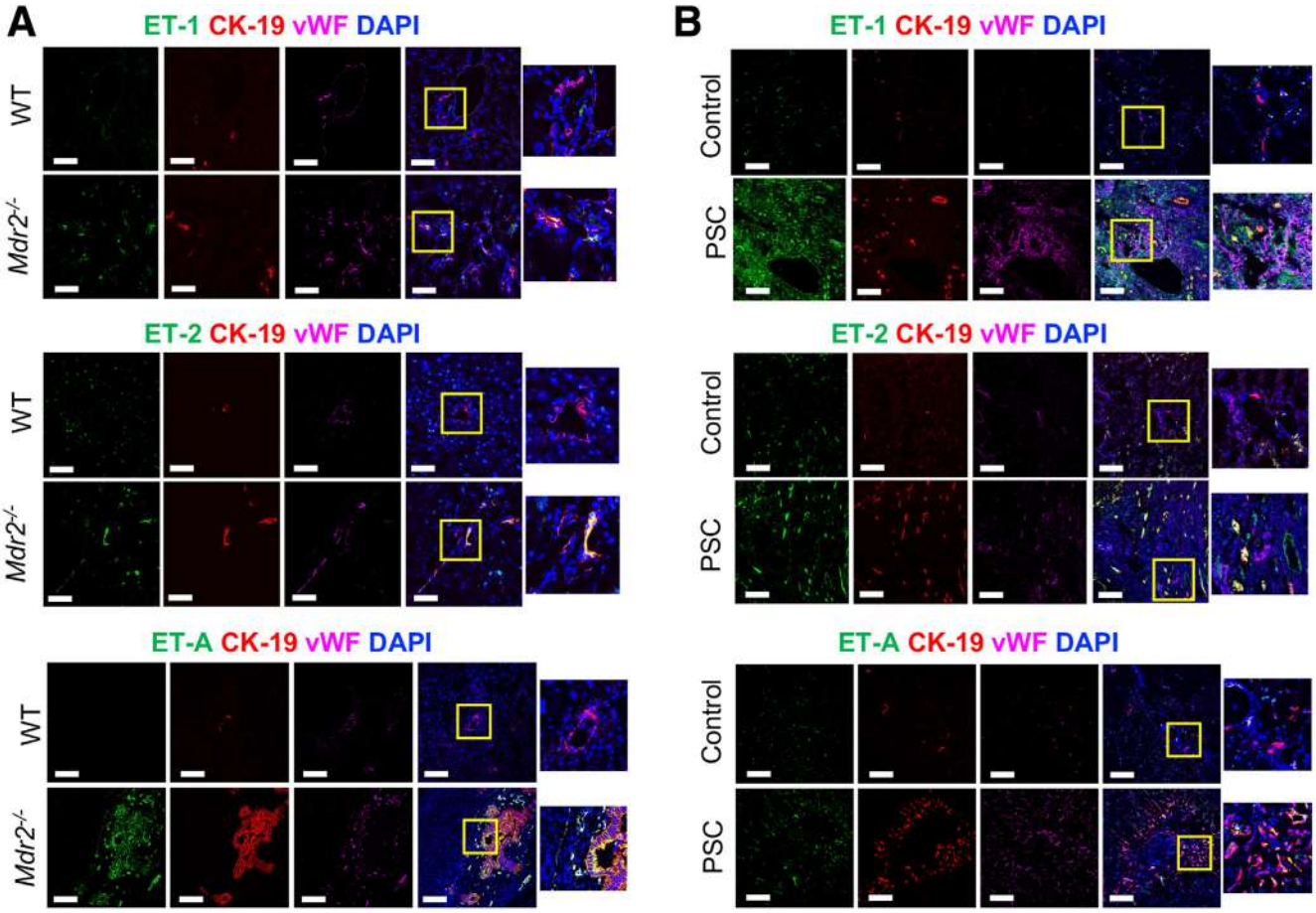

Figure 3. ET-1, ET-2, and ET-A expression in cholangiocytes and endothelial cells. (*A*) Co-staining for ET-1, ET-2, or ET-A with CK-19 and vWF in mouse samples. (*B*) Co-staining for ET-1, ET-2, or ET-A with CK-19 and vWF in human samples. Staining is 20× and 40×, scale bar = 116 μm.

biliary senescence were noted in treated WT mice versus controls or DMSO-treated *Mdr2*$^{-/-}$ mice versus controls (Figure 5*A*–*C*).

Immune Cell Infiltration and Inflammation Are Abrogated in Ambrisentan-Treated Mdr2$^{-/-}$ *Mice*

Macrophage infiltration is associated with angiogenesis in models of liver fibrosis,[16] and macrophage number was enhanced in *Mdr2*$^{-/-}$ mice compared with WT; however, macrophage number decreased in Ambrisentan-treated *Mdr2*$^{-/-}$ mice (Figure 6*A*). Similarly, T-cell (CD3+) and B-cell infiltration (CD20+) increased in *Mdr2*$^{-/-}$ mice compared with WT but were significantly reduced in Ambrisentan-treated *Mdr2*$^{-/-}$ mice (Figure 6*B* and *C*). No significant changes were found for macrophage, T-cell, or B-cell infiltration in treated WT mice versus controls or DMSO-treated *Mdr2*$^{-/-}$ mice versus controls (Figure 6*A*–*C*). We further confirmed changes in inflammatory signaling molecules, *Ccl2* and *Ccl5*, which were up-regulated in *Mdr2*$^{-/-}$ mice compared with WT but reduced in *Mdr2*$^{-/-}$ mice treated with Ambrisentan (Figure 6*D*).

Liver Fibrosis Is Reduced in Ambrisentan-Treated Mdr2$^{-/-}$ *Mice*

Liver fibrosis is associated with angiogenesis in a model of cirrhosis.[17] *Mdr2*$^{-/-}$ mice had increased collagen deposition and collagen, type I, α 1 (*Col1a1*) levels compared with WT, which were reduced in Ambrisentan-treated *Mdr2*$^{-/-}$ mice (Figure 7*A* and *B*). Fibrosis findings were confirmed by hydroxyproline levels and Masson's trichrome staining (Figure 7*C* and *D*). *Mdr2*$^{-/-}$ mice presented with ductular reaction extending away from the portal tracts and was embedded in areas of bridging fibrosis; however, this association was not noted in Ambrisentan-treated *Mdr2*$^{-/-}$ mice (Figure 7*E*). HSC presence increased in *Mdr2*$^{-/-}$ mice compared with WT but reduced in Ambrisentan-treated *Mdr2*$^{-/-}$ mice (Figure 7*F*). Collagen deposition and HSC presence were unchanged in treated WT mice versus controls and DMSO-treated *Mdr2*$^{-/-}$ mice versus controls, although DMSO-treated *Mdr2*$^{-/-}$ mice had significantly reduced *Col1a1* expression compared with controls (Figure 7*A*–*F*), which may be due to differential mRNA and protein expression levels due to post-transcriptional modifications.[18]

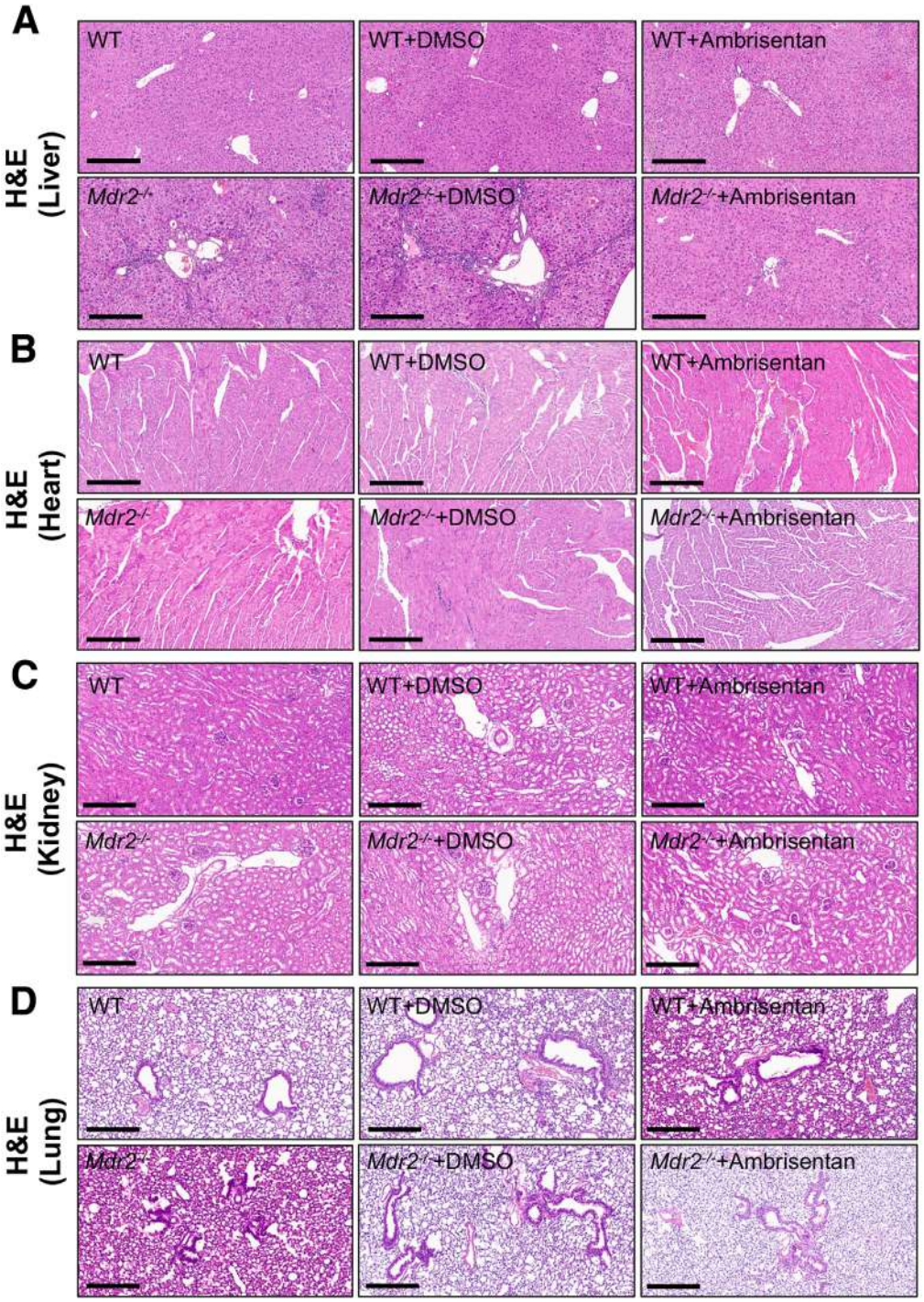

Figure 4. Tissue histology after Ambrisentan treatment. H&E staining in (*A*) liver, (*B*) heart, (*C*) kidney, and (*D*) lung in mouse samples. Staining is 10×, scale bar = 300 μm.

Vascular Endothelial Growth Factor-A Expression and Angiogenesis Are Decreased in Ambrisentan-Treated Mdr2$^{-/-}$ *Mice*

Anti-angiogenic treatment reduces vessel density and liver fibrosis in a model of cirrhosis[19]; therefore, we evaluated changes in angiogenesis in our model. Vascular endothelial growth factor-A (VEGF-A) expression was enhanced in the bile ducts of *Mdr2*$^{-/-}$ mice compared with WT; however, biliary VEGF-A expression was reduced in Ambrisentan-treated *Mdr2*$^{-/-}$ mice (Figure 8*A*). Similarly, the bile ducts of human PSC had increased VEGF-A expression compared with control (Figure 8*B*). The mRNA expression of *Vegfa* was enhanced in *Mdr2*$^{-/-}$ mice compared with WT but reduced in *Mdr2*$^{-/-}$ mice treated with Ambrisentan (Figure 9*A*). VEGF-A homodimers were increased in *Mdr2*$^{-/-}$ mice compared with WT but reduced in Ambrisentan-treated *Mdr2*$^{-/-}$ mice (Figure 9*B*). Interestingly, we detected VEGF-A potentially involved in heterodimers with

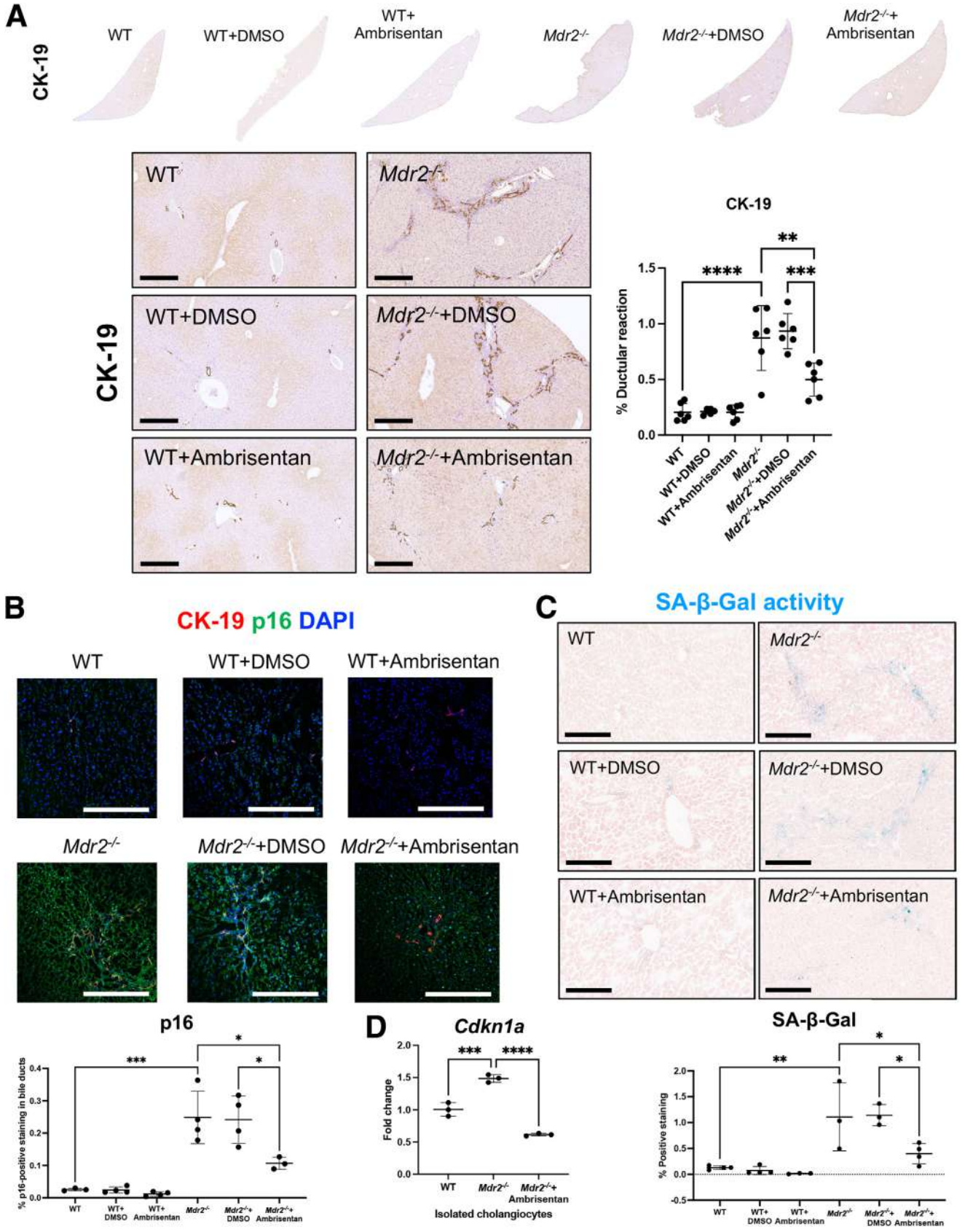
A
CK-19
WT
WT+DMSO
WT+ Ambrisentan
Mdr2-/-
Mdr2-/-+DMSO
Mdr2-/-+ Ambrisentan
WT+Ambrisentan
Mdr2-/-+Ambrisentan
CK-19
% Ductular reaction
****
**
***
B
CK-19 p16 DAPI
C
SA-β-Gal activity
p16
% p16-positive staining in bile ducts
D
Cdkn1a
Fold change
Isolated cholangiocytes
SA-β-Gal
% Positive staining

placental growth factor (PlGF).[20] VEGF-A potential heterodimers with PlGF were reduced in *Mdr2*$^{-/-}$ mice and unchanged with Ambrisentan treatment (Figure 9*B*). Like our mouse models, VEGF-A potential involvement in PlGF heterodimers was reduced in PSC compared with controls; however, VEGF-A homodimers were significantly increased in PSC compared with controls (Figure 9*C*). VEGF-A homodimers induce mitogenesis and angiogenesis via activation of VEGFR1 and VEGFR2.[21] Similarly, VEGF-A-PlGF heterodimers bind to VEGFR1 and VEGFR2 but have lower mitogenic and angiogenic capabilities.[20] These findings suggest that ET-A activity may modulate VEGF-A synthesis that is mainly involved in VEGF-A homodimeric signaling.

Vessel number (red arrowheads) increased near bile ducts in *Mdr2*$^{-/-}$ mice; however, vessel number was reduced after Ambrisentan treatment (Figure 8*C*). Changes in portal angiogenesis were confirmed by vWF/cytokeratin-19 (CK-19) immunostaining (Figure 8*D*). Changes in the above parameters were not noted in treated WT mice or DMSO-treated *Mdr2*$^{-/-}$ mice compared with controls (Figure 8*A* and *C*). Because no significant changes are found in treated WT mice and *Mdr2*$^{-/-}$ mice treated with DMSO, we reduced our models to WT, *Mdr2*$^{-/-}$, and *Mdr2*$^{-/-}$ + Ambrisentan mice for the remainder of our studies.

We wanted to understand whether angiogenesis correlated with other parameters of injury, so we used Pearson correlation to generate a correlation matrix. We found strong and significant positive correlations between angiogenesis (CD31), fibrosis (Sirius Red/Fast Green), ductular reaction (CK-19), and immune cell infiltration (CD3, CD20, F4/80) in WT and *Mdr2*$^{-/-}$ mice; no correlations were found for VEGF-A expression (Figure 8*E*). Direct correlations between these factors and angiogenesis or ductular reaction were plotted on a linear scale (Figure 8*F*). These findings suggest that angiogenesis and ductular reaction may worsen pathologic outcomes during PSC.

Compromised Biliary Epithelial Cell Integrity, Arteriole Dilation, and Loss of Endothelial Cilia Are Reversed in Ambrisentan-Treated Mdr2$^{-/-}$ Mice

We found expansive bile duct branching, indicative of ductular reaction, in *Mdr2*$^{-/-}$ mice, which is visualized by the degree of ink perfusion into the IH biliary tree (Figure 10*A*). However, bile duct branching was reduced in Ambrisentan-treated *Mdr2*$^{-/-}$ mice, which is demonstrated by less ink perfusion into the IH bile ducts (Figure 10*A*). Looking at ultrastructural components, transmission electron microscopy (TEM) imaging demonstrated that cholangiocytes (blue) had a squamous appearance with loss of microvilli and significant detachment from the basement membrane; however, Ambrisentan-treated *Mdr2*$^{-/-}$ mice cholangiocytes demonstrated a columnar structure and reformation of the microvilli, which is comparable to WT mice (Figure 10*B*). Basement membrane detachment was not affected by Ambrisentan treatment (Figure 10*B*). Arterioles (pink) were pushed further from bile ducts and showed loss of endothelial cilia (arrows) in *Mdr2*$^{-/-}$ mice, but these alterations were reversed in *Mdr2*$^{-/-}$ mice treated with Ambrisentan (Figure 10*B*). There is an apparent association between biliary damage and vascular integrity that may promote damage during cholestasis.

Cholangiocyte-Derived Angiocrine Factors Are Dependent on ET-A Signaling in Mdr2$^{-/-}$ Mice

We performed an angiogenesis array using cholangiocyte supernatants to evaluate biliary-derived angiogenic components. Cholangiocytes from *Mdr2*$^{-/-}$ mice had increased interleukin 6 (IL-6) secretion, which was reduced in Ambrisentan-treated *Mdr2*$^{-/-}$ mice (Figure 10*C*). Endothelial cells do not express the IL-6 receptor (IL-6R) and undergo IL-6 trans-signaling, which converges with transforming growth factor (TGF)-β1 pathways to promote inflammation.[22] *Mdr2*$^{-/-}$ mice had an increase in pro-angiogenic angiopoietin (*Angpt2)* hepatic expression; however, Ambrisentan reduced *Angpt2* but increased the vascular stabilizing *Angpt1*, demonstrating reduced vascular remodeling associated with angiogenesis (Figure 10*D*). Ingenuity Pathway Analysis (IPA) confirmed that ET-A activation reduces *Angpt1* but enhances *Angpt2* (Figure 10*E*).

Previous work has identified cholangiocytes as a major source of TGF-β1 and ET-1 in a model of hepatopulmonary syndrome.[23] IPA verified that ET-1/2 modulates TGF-β1 via ET-A, with no interaction with ET-B noted (Figure 9*D*). *Tgfb1* expression increased in the total liver and cholangiocytes isolated from *Mdr2*$^{-/-}$ mice and was reduced with Ambrisentan treatment (Figure 9*E* and *F*). TGF-β1 levels in cholangiocyte supernatants followed a similar trend (Figure 9*G*). There was enhanced immunoreactivity of TGF-β1 in cholangiocytes (white arrows) and endothelial cells (yellow arrows) in *Mdr2*$^{-/-}$ mice that was reduced after Ambrisentan treatment (Figure 9*H*). PSC patients had increased TGF-β1 immunoreactivity in cholangiocytes and endothelial cells (Figure 9*I*). Confirming this, *TGFB1* expression in isolated cholangiocytes is enhanced in PSC versus control (Figure 9*J*). During PSC, ET-A activation may promote TGF-β1 synthesis and secretion.

To demonstrate novel angiogenic factor signaling in cholangiocytes that is mediated by ET-A, we performed a

Figure 5. (***See previous page***). **Ductular reaction and biliary senescence after Ambrisentan treatment.** (*A*) Staining and semiquantification of CK-19 in mouse samples. (*B*) Co-staining for p16 and CK-19 in mouse samples and semiquantification. (*C*) SA-β-Gal activity in mouse samples. (*D*) *q*PCR for *Cdkn1a* in isolated cholangiocytes from mouse samples. Data are mean ± standard deviation. n = 4–5 portal areas per mouse imaged from n = 6 mice per group for CK-19; n = 3–5 portal areas imaged from n = 3–4 mice per group for p16/CK-19; n = 3–5 portal areas per mouse imaged from n = 3–4 mice per group for SA-β-Gal; n = 3 reactions per group in total RNA isolated from isolated cholangiocytes from n = 8 mice per group. CK-19 is 1× and 10×, scale bar = 300 μm; p16/CK-19 is 20×, scale bar = 250 μm; SA-β-Gal is 20×, scale bar = 200 μm. *$P < .05$, **$P < .01$, ***$P < .001$, ****$P < .0001$.

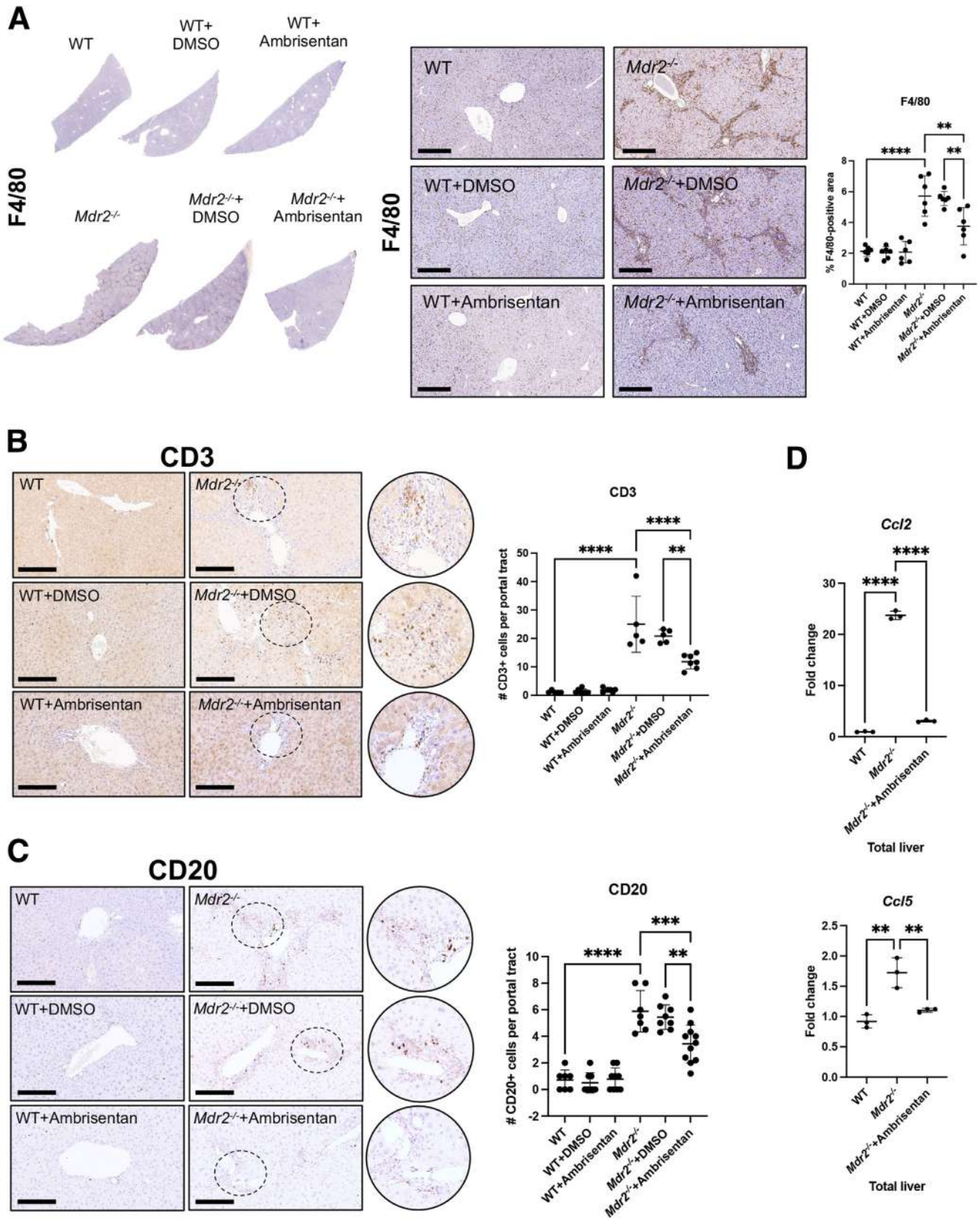

Figure 6. Immune cell infiltration and inflammation after Ambrisentan treatment. (*A*) F4/80 staining and semiquantification in mouse samples. (*B*) CD3 staining and semiquantification in mouse samples. (*C*) CD20 staining and semiquantification in mouse samples. (*D*) *Ccl2* and *Ccl5* mRNA expression in total liver. Data are mean ± standard deviation. n = 4–5 portal areas per mouse imaged from n = 6 mice per group for F4/80; n = 10 portal areas per mouse imaged from n = 6–11 mice per group for CD3 and CD20. n = 3 reactions per group in total RNA isolated from n = 6 mice per group. F4/80 is 1× and 10×, scale bar = 300 μm; CD3 and CD20 are 20× and 40×; scale bar = 200 μm. *$P < .05$, **$P < .01$, ***$P < .001$, ****$P < .0001$.

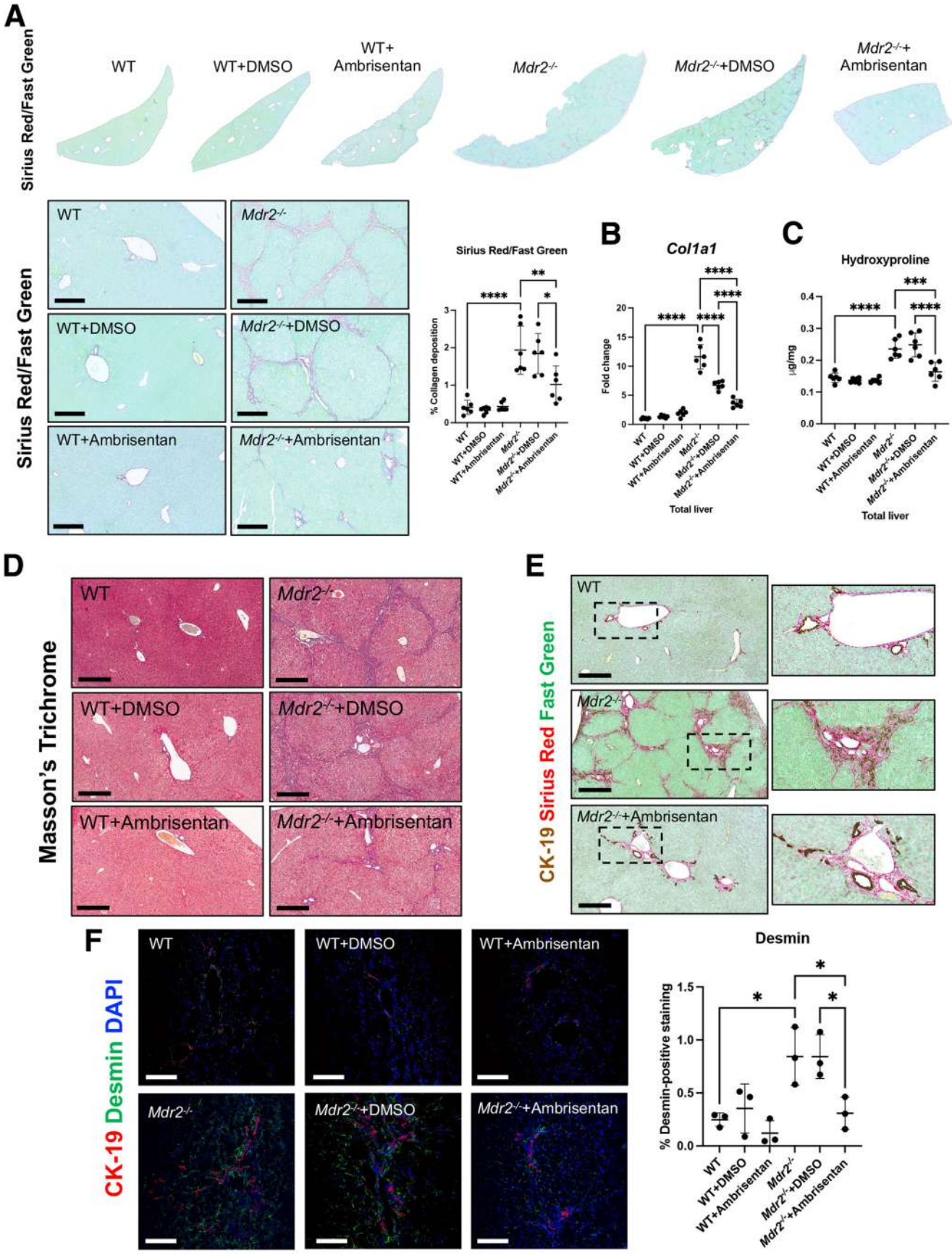
A
Sirius Red/Fast Green
WT
WT+DMSO
WT+ Ambrisentan
Mdr2-/-
Mdr2-/-+DMSO
Mdr2-/-+ Ambrisentan
Sirius Red/Fast Green
WT
Mdr2-/-
WT+DMSO
Mdr2-/-+DMSO
WT+Ambrisentan
Mdr2-/-+Ambrisentan
Sirius Red/Fast Green
% Collagen deposition
B
Col1a1
Fold change
Total liver
C
Hydroxyproline
µg/mg
Total liver
D
Masson's Trichrome
WT
Mdr2-/-
WT+DMSO
Mdr2-/-+DMSO
WT+Ambrisentan
Mdr2-/-+Ambrisentan
E
CK-19 Sirius Red Fast Green
WT
Mdr2-/-
Mdr2-/-+Ambrisentan
F
CK-19 Desmin DAPI
WT
WT+DMSO
WT+Ambrisentan
Mdr2-/-
Mdr2-/-+DMSO
Mdr2-/-+Ambrisentan
Desmin
% Desmin-positive staining

polymerase chain reaction (PCR) array in isolated cholangiocytes. We found that midkine (*Mdk*) expression was significantly up-regulated in isolated cholangiocytes from *Mdr2*$^{-/-}$ mice compared with WT, which was reversed with Ambrisentan treatment (Figure 11*A*). Because the role of Mdk has not been studied in cholangiocytes, cholestasis, or PSC previously, we focused on this gene. We confirmed biliary changes of *Mdk* by quantitative PCR (*q*PCR) (Figure 11*B*). Mdk biliary immunoreactivity increased in *Mdr2*$^{-/-}$ mice compared with WT but decreased with Ambrisentan treatment (Figure 11*C*). Human PSC had enhanced biliary Mdk immunoreactivity compared with control (Figure 11*D*). We found that Mdk expression is enhanced in cholangiocytes (CK-19), portal vascular endothelial cells (vWF), macrophages (F4/80), and HSCs (desmin) but not hepatocytes (HNF4α) of *Mdr2*$^{-/-}$ mice compared with controls (Figure 12).

Ambrisentan Treatment Reduces Biliary Mdk Expression Through Fos Proto-oncogene

We first performed IPA to evaluate links between ET-A and IL-6, TGF-β1, and Mdk. When looking for direct downstream factors, we found that the transcription factor FOS (ie, Fos proto-oncogene [cFOS]) was the only factor to have multiple connections, specifically to IL-6 and TGF-β1 with a link to Mdk unknown (Figure 11*E*). ET-1/ET-A induction of TGFB1 and IL-6 synthesis has been previously published,[24,25] and considering that IPA pulls its data from publicly available information, it may be that cFOS/*MDK* binding is unknown. For this reason, we used PROMO to predict cFOS binding to the promoter region of *MDK* and found a binding site within the promoter region of *MDK* with low dissimilarity and low chance of random expectation (Figure 11*F*). We evaluated changes in cFOS by Western blotting, and interestingly we found no changes in total cFOS but increased levels of phospho-Fos proto-oncogene (p-cFOS) in *Mdr2*$^{-/-}$ mice compared with WT, but reduced p-cFOS in *Mdr2*$^{-/-}$ mice treated with Ambrisentan (Figure 11*G*). Interestingly, phosphorylation of cFOS enhances its transcriptional ability.[26] Changes in biliary p-cFOS expression were confirmed by immunostaining (Figure 11*H*).

ET-1/ET-A Signaling Influence on Different Cells, In Vitro

In *Mdr2*$^{-/-}$ mice, Ambrisentan treatment decreased ductular reaction, portal angiogenesis, immune cell infiltration. and liver fibrosis; therefore, we performed *in vitro* experiments to understand which cell type is affected by ET-1/ET-A signaling. *In vitro*, ET-1 induced human intrahepatic biliary epithelial cell (HIBEC) senescence, which was blocked by Ambrisentan pretreatment (Figure 13*A* and *B*). *In vitro*, human hepatic stellate cells (hHSCs) did not increase fibrogenesis after ET-1 or Ambrisentan treatment (Figure 13*C* and *D*). Interestingly, *in vitro* treatment of human umbilical vein endothelial cells (HUVECs) with ET-1 increased angiogenesis, but this was unaffected by Ambrisentan pretreatment (Figure 13*E* and *F*). *In vitro*, ET-1 and Ambrisentan treatment did not induce hHEP senescence or proliferation (Figure 13*G* and *H*), which may explain our finding that Ambrisentan did not alter lobular inflammation or necrosis (Figure 4*A*). Lastly, *in vitro* treatment of THP-1 (differentiated to macrophages) with ET-1 induced inflammation, which was blocked by Ambrisentan pretreatment (Figure 13*I* and *J*).

Ambrisentan Treatment Blocks HUVEC Migration, In Vitro

Cholangiocyte purity in control (n = 3) and PSC (n = 3) samples was confirmed by CK-19 immunostaining (Figure 14*A*). Although >70% of cells were CK-19+, the expression of CK-19 appears lower in EH cholangiocytes compared with IH cholangiocytes, and differential CK-19 expression based on location in the biliary tree has been demonstrated previously.[27] We treated control and PSC cholangiocytes with Ambrisentan or vehicle (DMSO) and determined that treatment did not alter cellular morphology (Figure 14*B*). We stimulated HUVECs with supernatants combined from all treated cholangiocytes (experimental outline, Figure 14*C*) and found that DMSO-treated PSC cholangiocytes enhanced HUVEC migration compared with control; however, HUVECs stimulated with Ambrisentan-treated PSC cholangiocyte supernatants had reduced migration (Figure 14*D*). These data demonstrate that biliary-derived factors promote angiogenic processes in endothelial cells.

Discussion

ET-A antagonism diminishes biliary and liver damage associated with cholangitis in *Mdr2*$^{-/-}$ mice. Reductions in ductular reaction and biliary senescence suggest that ET-A may modulate cholangiocyte damage and angiogenesis through autocrine and paracrine mechanisms. We found that biliary expression of IL-6, TGF-β1, and Mdk, which are known to contribute to angiogenesis and vascular remodeling, are enhanced, which demonstrates a close

Figure 7. (***See previous page***). **Liver fibrosis after Ambrisentan treatment.** (*A*) Sirius Red/Fast Green staining and semi-quantification in mouse samples. (*B*) *Col1a1* mRNA expression in total liver from mouse samples. (*C*) Hydroxyproline content in mouse samples. (*D*) Masson's trichrome staining in mouse samples. (*E*) Co-staining for CK-19 and Sirius Red/Fast Green in mouse samples. (*F*) Co-staining for CK-19 and desmin in mouse samples. Data are mean ± standard deviation. n = 4–5 portal areas per mouse imaged from n = 6 mice per group for Sirius Red/Fast Green; n = 6 reactions per group in total RNA isolated from n = 6 mice; n = 3 reactions per mouse from n = 6 mice per group for hydroxyproline; n = 3 portal areas per mouse imaged from n = 3 mice per group for desmin. Sirius Red/Fast Green is 1× and 10×, scale bar = 300 μm; Masson's trichrome is 10×, scale bar = 300 μm; CK-19/Sirius Red/Fast Green is 10× and 30×, scale bar = 300 μm; CK-19/desmin is 20×, scale bar = 116 μm. *$P < .05$, **$P < .01$, ***$P < .001$, ****$P < .0001$.

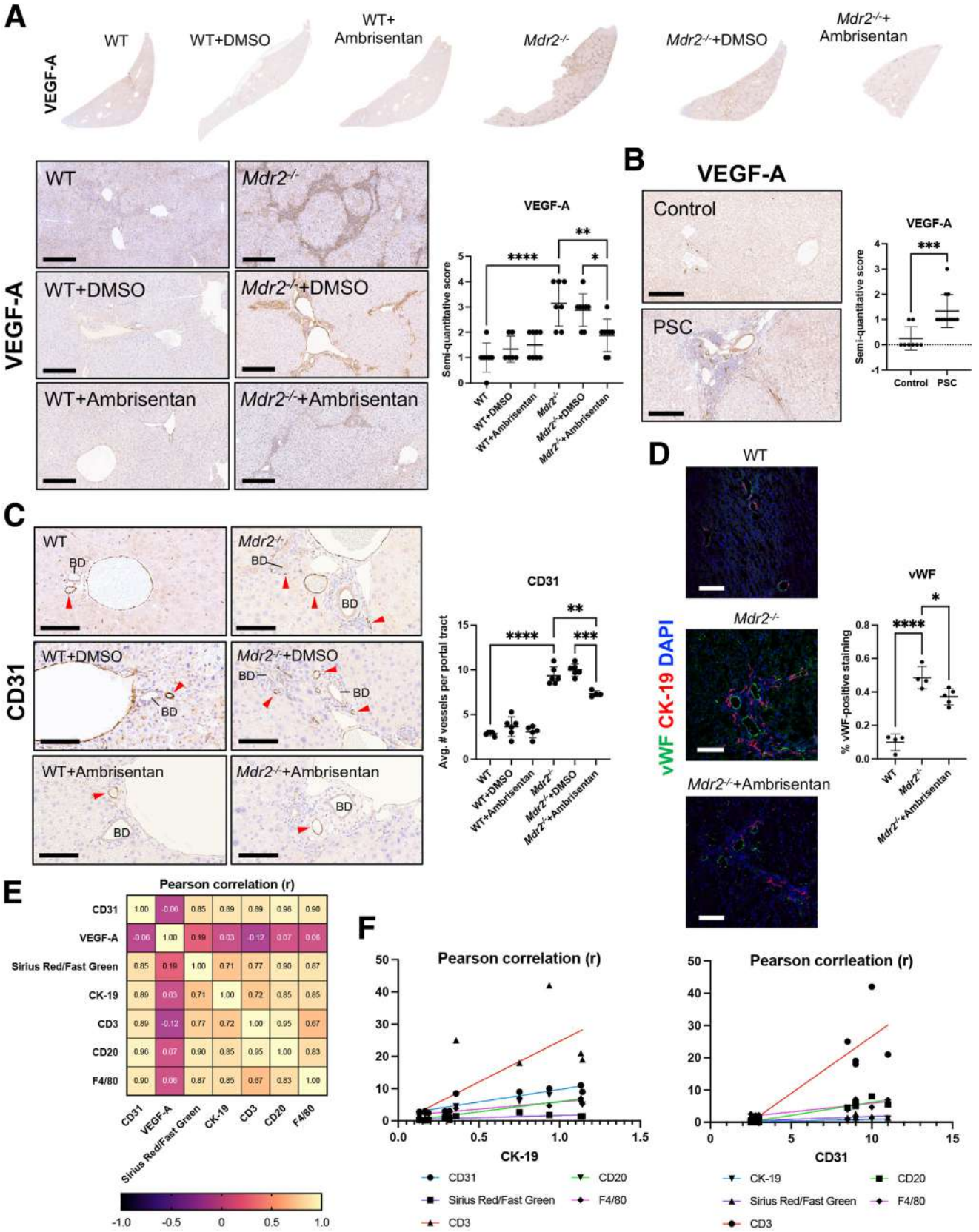
A
VEGF-A
WT
WT+DMSO
WT+ Ambrisentan
Mdr2-/-
Mdr2-/-+DMSO
Mdr2-/-+ Ambrisentan
WT+Ambrisentan
Mdr2-/-+Ambrisentan
VEGF-A
Semi-quantitative score
****
**
*
B
VEGF-A
Control
PSC
***
Control
PSC
C
CD31
BD
Avg. # vessels per portal tract
D
WT
Mdr2-/-
Mdr2-/-+Ambrisentan
vWF CK-19 DAPI
vWF
% vWF-positive staining
E
Pearson correlation (r)
CD31 1.00 -0.06 0.85 0.89 0.89 0.96 0.90
VEGF-A -0.06 1.00 0.19 0.03 -0.12 0.07 0.06
Sirius Red/Fast Green 0.85 0.19 1.00 0.71 0.77 0.90 0.87
CK-19 0.89 0.03 0.71 1.00 0.72 0.85 0.85
CD3 0.89 -0.12 0.77 0.72 1.00 0.95 0.67
CD20 0.96 0.07 0.90 0.85 0.95 1.00 0.83
F4/80 0.90 0.06 0.87 0.85 0.67 0.83 1.00
F
Pearson correlation (r)
CK-19
Pearson correlation (r)
CD31
CD31
CD20
Sirius Red/Fast Green
F4/80
CD3

relationship between cholangiocytes and endothelial cells. Our findings suggest that cholangiocytes contribute to angiogenesis via ET-A–dependent signaling, and angiogenesis may be a pathogenic mechanism in PSC.

ET-A antagonism reduces portal damage, including ductular reaction, and biliary senescence. After BDL, cholangiocytes are the main source of ET-1 and TGF-β1, which significantly correlate with one another.[23] ET-1 induces cholestasis alongside portal pressure in normal rats.[13,14] In cirrhotic humans, ET-1 levels in hepatic venous blood significantly correlated with bile duct volume,[28] suggesting that ET-1 promotes ductular reaction. However, the impact of ET-A inhibition on biliary damage in PSC or other cholestatic models is unknown. Our findings show that blocking ET-A inhibits ductular reaction and biliary damage in *Mdr2*$^{-/-}$ mice.

An interesting finding in our study was the discrepancy in ET-1 and ET-2 levels in humans and mice. Secretion of ET-1 and ET-2 was enhanced in *Mdr2*$^{-/-}$ mice, but only ET-1 levels increased in human PSC. Murine ET-2 (also termed vasoactive intestinal contractor) is orthologous to the human ET-2,[29] with the peptide differing by 1 amino acid.[30] *In vitro* studies have shown that vasoactive intestinal contractor is 40-fold weaker than human ET-2 in inducing contractions in human vascular smooth muscle cells,[31] showing species-specific mechanisms. Colonic ET-2 expression and secretion are unaffected in humans with ulcerative colitis or inflammatory bowel disease, but colonic ET-2 levels are enhanced in a mouse model of experimental inflammatory bowel disease.[32] Species-specific differences in vasoactive intestinal contractor and human ET-2 functionality may lend to differing concentrations in *Mdr2*$^{-/-}$ mice and human PSC. In addition, levels of *END1*, *END2*, *ENDRA,* and *TGFB1* vary in our human PSC cholangiocytes, which may be due to individual variability[33,34] or the original location being IH or EH. It is known that various receptors and transporters can have differing levels of expression dependent on location in the biliary tree[27]; thus work evaluating heterogenous ET-A signaling in IH versus EH cholangiocytes is necessary.

ET-1 is a potent vasoconstrictor,[35] and overexpression of ET-1 in BDL rats contributes to portal hypertension.[36] ET-1 increases hepatic vascular resistance in a dose-dependent manner *in vivo*.[37] ET-A antagonist (BQ123) treatment reduced portal pressure and enhanced hepatic arterial blood flow in patients with cirrhosis[38] demonstrating the role of ET-A on the hepatic vasculature. In this small cohort, the administration of selective ET-A antagonists (BQ123 or Ambrisentan) decreased portal pressure in Child-Pugh B cirrhotic patients,[38] demonstrating the efficacy of ET-A inhibition in select cirrhotic patients. We found that blocking ET-A decreases angiogenesis and ductular reaction in *Mdr2*$^{-/-}$ mice, suggesting that ET-A may be important in the pathophysiology of cholangitis. Considering the above clinical trial and previous reports that *Mdr2*$^{-/-}$ mice present with portal hypertension,[39] we postulate that targeting ET-1/ET-A signaling in PSC may be a potential therapeutic, specifically for patients with cirrhosis or portal hypertension.

Ductular reaction contributes to damaging phenotypes in PSC through paracrine cell signaling.[2] We found a reduction in the peribiliary presence of macrophages, T cells, and B cells, as well as reduced liver fibrosis in *Mdr2*$^{-/-}$ mice treated with Ambrisentan. It is plausible that ET-A–mediated effects on biliary injury and secretion of chemoattractants contribute to inflammatory events and liver fibrosis. HSCs can be activated by ET-1 to promote collagen synthesis[40]; however, studies suggest that ET-1 preferentially signals through ET-B on HSCs that show desensitization to ET-A after activation.[41,42] One study found that ET-A antagonist treatment (LU-135252) reduces liver fibrosis in BDL rats but did not evaluate the cellular targets.[11] We presume that changes in fibrogenesis after ET-A inhibition in *Mdr2*$^{-/-}$ mice may be due to paracrine signaling from cholangiocytes or endothelial cells. Inflammatory macrophages express ET-1,[42,43] and ET-1 is pro-inflammatory in B cells and T cells via ET-A and ET-B activity.[44] Therefore, ET-A inhibition may act on immune cells directly to modulate their activation, but considering their proximity with bile ducts, their influx may be influenced by biliary ET-A activity as well.

Ductular reaction correlates with angiogenesis and angiocrine signaling in hepatitis C virus infected patients.[45] Cholangiocyte- and myofibroblast-derived VEGF-A laden microparticles induce angiogenesis in cirrhotic humans.[46] Ductular reaction promotes intrahepatic angiogenesis in 3,5-diethoxycarbonyl-1,4-dihydrocollidine–fed mice via Slit-2/Roundabout-1 signaling.[4] In *Mdr2*$^{-/-}$ mice, progressive peribiliary fibrosis leads to separation of the PVP from the bile ducts as early as 4 weeks of age, a phenotype seen in our models, and PVP separation may contribute to bile duct atrophy.[47] Indeed, bile ducts and the vasculature communicate closely with one another, and their individual health is dependent on one another. We propose that biliary-endothelial crosstalk can be partially attributed to ET-A–dependent angiocrine signals.

The pathophysiological relevance of angiogenesis during liver injury is under debate, with its role as a wound-healing versus pathogenic mechanism argued. We found that inhibition of ET-A was able to increase hepatic *Angpt1* (vessel stabilizing) but reduced hepatic *Angpt2* (pro-angiogenic)

Figure 8. (***See previous page***). **Angiogenesis after Ambrisentan treatment and correlation analyses.** VEGF-A staining and semiquantitative score in (*A*) mouse samples and (*B*) human samples. (*C*) CD31 staining and semiquantification in mouse samples. (*D*) Co-staining for vWF and CK-19 in mouse samples. (*E*) Pearson correlation matrix for WT and *Mdr2*$^{-/-}$ mice. (*F*) Pearson correlation for histopathologic parameters versus CK-19 and CD31. Data are mean ± standard deviation. n = 10 portal areas scored from n = 6–8 mice per group, n = 8 human control, and n = 12 human PSC for VEGF-A; n = 6 mice per group analyzed for correlation; n = 10 portal areas imaged from n = 4–6 mice per group for CD31; n = 3–5 portal areas imaged from n = 4–5 mice per group for vWF. VEGF-A is 1× and 10×, scale bar = 300 μm; CD31 is 40×, scale bar = 200 μm; vWF/CK-19 is 20×, scale bar = 75 μm. *$P < .05$, **$P < .01$, ***$P < .001$, ****$P < .0001$.

expression through TGF-β1. ET-1 can directly decrease *Angpt1* expression[48] but can also promote *TGFB1* gene expression,[49] which in turn reduces *Angpt1* gene expression.[50] Interestingly, increased TGF-β1 levels are associated with enhanced VEGF-A,[51,52] which in turn promotes *Angpt2* expression.[53] Last, Angpt1 can down-regulate

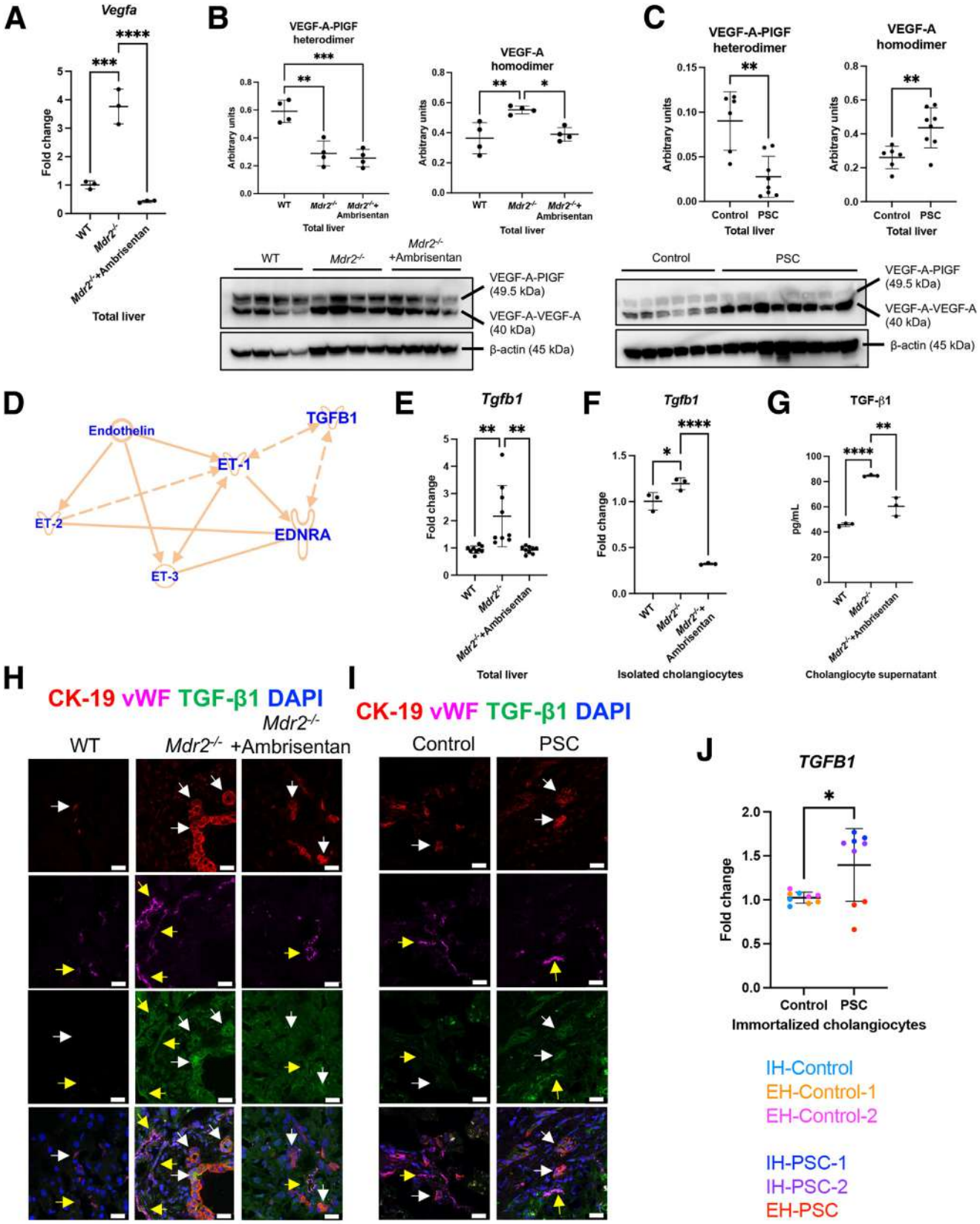

Angpt2 release.[54,55] Therefore, in injured *Mdr2*$^{-/-}$ mice, blocking ET-A may promote vessel stabilization and block angiogenesis through differential regulation of *Angpt1* and *Angpt2*. When further looking at angiogenic signaling, we found that biliary-derived TGF-β1, IL-6, and Mdk (known to promote angiogenesis) were increased, and inhibition of ET-A reduced the expression of these factors. In aortic endothelial cells, TGF-β1 levels are pro-inflammatory and correspond with loss of endothelial cilia[56]; therefore, the loss of endothelial cilia noted in our mice may be suggestive of damage. Biliary IL-6 is a senescence-associated secretory phenotype factor in PSC[57] and a dynamic component of portal hypertension development.[3] IL-6 promotes abnormal angiogenesis that may give rise to inflammatory diseases.[58] Mdk induces neovascularization under hypoxic conditions[59] and enhances arteriogenesis through increased VEGF-A levels.[60] Previous studies demonstrate a connection between TGF-β1/IL-6[22]; therefore, the convergence of these pathways demonstrates a biliary-specific angiocrine signature that may regulate angiogenesis in PSC.

Although our study focused on ET-A–dependent signaling mechanisms and angiocrine release in cholangiocytes, this pathway may be affecting other cell types. Our *in vitro* studies found that ET-1 induced cholangiocyte senescence, HUVEC angiogenesis, and macrophage inflammation; however, changes in cholangiocytes and macrophages were blocked by Ambrisentan pretreatment. It has been shown that ET-1 induces endothelial cell angiogenesis, specifically VEGF-A expression, via ET-B, which may be why we did not see changes with Ambrisentan treatment.[61] However, it is important to note that HUVECs are derived from the umbilical vein and may not accurately reflect how liver-resident endothelial cells may respond to ET-1/ET-A. Furthermore, the THP-1 cells are circulating monocytes that were differentiated to macrophages using PMA treatment, so although they may recapitulate how infiltrating macrophages may respond to ET-1/ET-A, they may have a different cellular response than what liver-resident macrophages may have to ET-1/ET-A signaling. We also found that ET-1/ET-A did not affect HSC fibrogenesis, which is supported by findings that activated HSCs reduce ET-A but increase ET-B expression.[49] One caveat is that hHSCs are activated in culture; therefore, although our ET-1 stimulations did not enhance fibrogenesis, it does not determine whether ET-1 may be able to initiate HSC activation. Future work with quiescent HSCs and better *in vivo* tools will be necessary to tease out the potential initiating role of ET-1/ET-A on HSCs. Ambrisentan treatment did not change lobular inflammation or necrosis in *Mdr2*$^{-/-}$ mice, and *in vitro* ET-1/ET-A did not affect hepatocyte senescence or proliferation. Others have found that ET-A inhibition does not protect hepatocytes from tumor necrosis factor-α– or oxidative stress–induced damage *in vitro*.[62] Also, Mdk expression was enhanced in cholangiocytes, endothelial cells, macrophages, and HSCs in *Mdr2*$^{-/-}$ mice but not in hepatocytes. Macrophage-derived Mdk promotes endothelial proliferation,[63] and activated HSCs increase Mdk expression.[64] Changes in Mdk may be directly modulated by ET-A in some cells but may also be an indirect consequence. More studies are required for cell-specific changes in ET-A and Mdk.

Our findings suggest that Ambrisentan, an anti-angiogenic modulator, may be a therapeutic option for PSC patients. Telmisartan is an angiotensin II type 1 receptor antagonist and an anti-angiogenic therapeutic.[65] One study found that Telmisartan was unable to reduce liver fibrosis in *Mdr2*$^{-/-}$ mice after 3 months of treatment.[65] Oppositely, Telmisartan reduced liver fibrosis but not inflammation in rats subjected to BDL for 4 weeks.[66] Compared with our study, these findings suggest Telmisartan may reduce liver fibrosis, but not inflammation, in certain models. The integrin αVβ3 is mainly expressed on endothelial cells[67] and is important for VEGF-mediated pathologic angiogenesis.[68] Cilengitide is a specific αVβ3 inhibitor and was shown to reduce angiogenesis but exacerbate liver fibrosis in BDL and thioacetamide-treated rats.[69] Cilengitide may preferentially target hepatic endothelial cells, unlike Ambrisentan that may have a role on endothelial cells, cholangiocytes, and infiltrating immune cells, leading to these differences in outcomes. Considering that ET-1 induces cholestasis via ET-A on large cholangiocytes,[70] there may be other roles for Ambrisentan aside from anti-angiogenesis that mediate the benefits seen in *Mdr2*$^{-/-}$ mice in our study compared with other studies using angiogenic blockers.

Our study demonstrates that ET-1, ET-2, and ET-A are enhanced in *Mdr2*$^{-/-}$ mice and human PSC, but ET-1/ET-A may be the predominant and conserved mechanism regulating damage. This work suggests that angiogenesis in *Mdr2*$^{-/-}$ mice and PSC may be pathologic and promote damage due to abnormal alterations to the endothelium. We found that inhibition of ET-A reduced cholangiocyte expression of angiocrine factors in *Mdr2*$^{-/-}$ mice; therefore, targeting ET-A may prove therapeutic for PSC patients,

Figure 9. (***See previous page***). **VEGF-A and TGF-β1 signaling after Ambrisentan treatment.** (*A*) mRNA expression of *Vegfa* in total liver. Western blotting for VEGF-A in total liver from mouse models (*B*) and human samples (*C*). (*D*) IPA linking ET and TGF-β1. (*E*) *Tgfb1* mRNA expression in total liver and (*F*) isolated cholangiocytes from mouse models. (*G*) TGF-β1 levels in cholangiocyte supernatants from mouse models. (*H*) Co-staining for CK-19, vWF, and TGF-β1 in mouse models. (*I*) Co-staining for CK-19, vWF, and TGF-β1 in human samples. (*J*) *TGFB1* mRNA expression in human isolated cholangiocytes. Data are mean ± standard deviation. n = 3–9 reactions in total RNA isolated from total liver from n = 6 mice per group for *q*PCR; n = 3 reactions in total RNA isolated from cholangiocytes isolated from n = 8 mice per group for *q*PCR. n = 3 reactions per group in cholangiocyte supernatants pooled from n = 8 mice per group. n = 3 reactions per sample for *q*PCR in n = 3 control and n = 3 PSC cholangiocyte samples. n = 1 reaction per mouse in protein isolated from n = 4 mice per group for Western blot. n = 1 reaction per human in protein isolated from n = 5 human control and n = 7 human PSC. Staining is 80×, scale bar = 25 μm. *$P < .05$, **$P < .01$, ***$P < .001$, ****$P < .0001$.

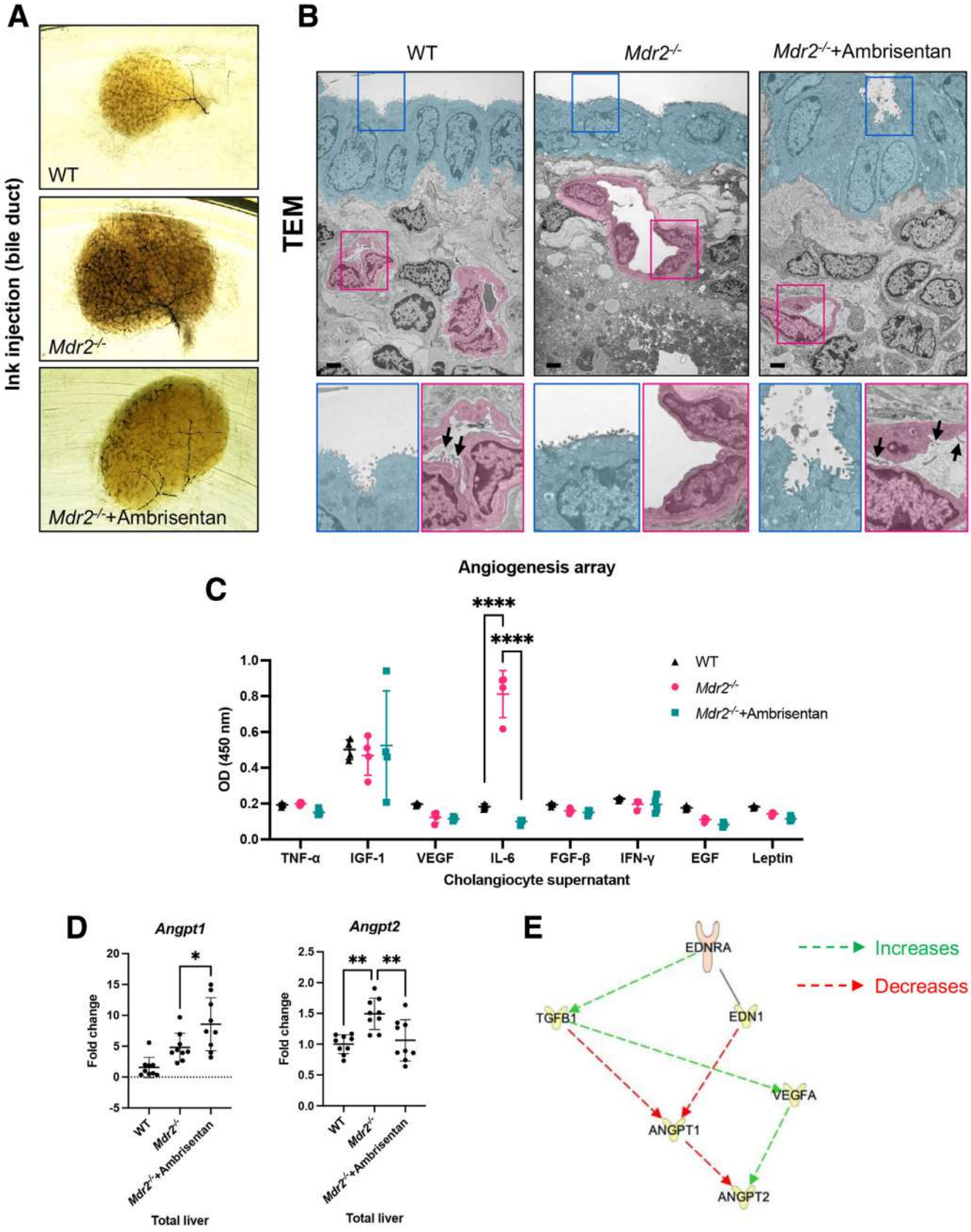
A
Ink injection (bile duct)
WT
Mdr2-/-
Mdr2-/-+Ambrisentan
B
TEM
WT
Mdr2-/-
Mdr2-/-+Ambrisentan
C
Angiogenesis array
OD (450 nm)
WT
Mdr2-/-
Mdr2-/-+Ambrisentan
TNF-α
IGF-1
VEGF
IL-6
FGF-β
IFN-γ
EGF
Leptin
Cholangiocyte supernatant
D
Angpt1
Angpt2
Fold change
Total liver
E
EDNRA
TGFB1
EDN1
VEGFA
ANGPT1
ANGPT2
Increases
Decreases

specifically those demonstrating vascular alterations or portal hypertension.

Materials and Methods

Materials and Equipment

Antibodies are detailed in Table 1. Formalin-fixed, paraffin-embedded (FFPE) and optimal cutting temperature (OCT) compound–embedded blocks were sectioned at 4–6 μm. Immunohistochemical stains were performed in FFPE sections, and immunofluorescent stains were performed in OCT compound–embedded sections. Immunohistochemical stains were scanned using the Leica Aperio AT2 System and imaged using the Leica Aperio ImageScope Software (Leica Biosystems; Buffalo Grove, IL). Immunofluorescent stains were imaged using the Leica TCS SP5 X System (Leica Biosystems; Buffalo Grove, IL).

Protein was extracted from snap-frozen total liver using RIPA buffer, and protein estimation was performed with the Thermo Scientific Pierce BCA Protein Assay Kit (Thermo Fisher Scientific, Waltham, MA). Protein samples were mixed with NuPAGELDS Sample Buffer (4×), run on Mini-PROTEAN TGX Precast Gels, and imaged with a ChemiDoc Imaging System, all from Bio-Rad Laboratories (Hercules, CA). Protein bands were visualized by enhanced chemiluminescence using Pierce enhanced chemiluminescence Western Blot Substrate (Thermo Fisher Scientific). Densitometry of bands was calculated with ImageJ (NIH).

Total RNA was isolated using the TRI Reagent from Sigma-Aldrich (St Louis, MO) and reverse transcribed using the iScript cDNA Synthesis Kit from Bio-Rad Laboratories for *q*PCR analysis. All primers were purchased from Qiagen (Valencia, CA) (Table 2) and were run using the iTaq Universal SYBR Green Supermix purchased from Bio-Rad Laboratories. For the PCR array, total RNA was reverse-transcribed using the RT^2 First Strand Kit, and PCR was performed with the RT^2 SYBR Green *q*PCR Mastermix both from Qiagen (Valencia, CA). Quantitative PCR and PCR array were run using the Applied Biosystems ViiA 7 Real-Time PCR System (Thermo Fisher Scientific).

Animal Models and Cholangiocyte Isolation

Animal procedures were performed in accordance with protocols approved by the Indiana University-Purdue University Indianapolis Institutional Animal Care and Use Committee. Male *Mdr2*$^{-/-}$mice (maintained in colony at our facility) at 12 weeks of age were subjected to daily intraperitoneal injections of Ambrisentan (ET-A antagonist, 5 mg/kg BW/day; Sigma-Aldrich) or vehicle (12.5% DMSO) for 1 week.[71] Age- and sex-matched WT (FVB/NJ strain) were purchased from the Jackson Laboratory (Bar Harbor, ME) and treated with Ambrisentan or 12.5% DMSO accordingly. In separate studies, male *Mdr2*$^{-/-}$ mice at 4, 8, and 12 weeks were used to analyze vascular changes. From all mice, the left lateral lobe was collected and divided into 3 pieces to generate snap-frozen, OCT-embedded, and FFPE liver samples. The section of the left lateral lobe that is most distal to the common bile duct was used for snap-frozen samples, the middle portion was used for OCT embedding, and the section most proximal to the common bile duct was used for FFPE sections. We collected liver and other organs, serum, IH cholangiocytes, and isolated IH cholangiocyte supernatants.[7] For cholangiocyte isolation, mouse livers were perfused with 1× HEPES-buffered saline containing 0.02% (wt/vol) egtazic acid until the liver was pale, demonstrating blood clearance. Liver perfusion continued but was then performed with a digestion solution composed of 1× HEPES-buffered saline containing 0.01% (wt/vol) $MgSO_4$, 0.02% (wt/vol) collagenase, and 3.4 mmol/L $CaCl_2$. After perfusion, the liver was collected in 1× HEPES-buffered saline and manually dissociated on ice with forceps. The liver pieces in 1× HEPES-buffered saline were then centrifuged at 1600 rpm at 4°C for 5 minutes; the lysate was discarded. The cell pellet was resuspended in a digestion buffer containing 5 mg/mL deoxyribonuclease I, 3.125 mg/mL collagenase, and 2.08 mg/mL hyaluronidase dissolved in RPMI 1640 medium in a shaking 37°C water bath for 20 minutes. Next, the cell suspension was centrifuged at 1600 rpm for 5 minutes at 4°C, and the lysate was discarded; the remaining pellet was washed with 1× HEPES-buffered saline and centrifuged again. The lysate was discarded, and the cell pellet was digested further with a buffer containing 1 mg/mL bovine pancreas trypsin dissolved in 1× phosphate-buffered saline/0.02% EDTA solution at 7.4 pH in a shaking 37°C water bath for 5 minutes. After 5 minutes, fetal bovine serum was added, and the cell suspension was digested in a shaking 37°C water bath for an additional 5 minutes. Next, the cell suspension was centrifuged at 1600 rpm for 5 minutes at 4°C, and the lysate was discarded; the remaining pellet was washed with 1× HEPES-buffered saline and centrifuged again. The lysate was discarded, and the pellet was resuspended in RPMI 1640 medium containing 5 mg/mL deoxyribonuclease I. The cell suspension was passed once through a 19-gauge needle and twice through a 22-gauge needle to break up clumps; the resulting cell suspension was filtered through a 100-μm cell strainer. The cells were then incubated on a rotator at 4°C for 30 minutes in an RPMI 1640 medium solution containing 5 mg/mL deoxyribonuclease and antibody-bound magnetic beads on a rotator at 4°C; the monoclonal antibody (IgG2a, from Dr R. Faris, Brown University, Providence, RI) is against an unidentified antigen expressed by IH

Figure 10. (***See previous page***). **Vascular and angiogenic changes after Ambrisentan treatment.** (*A*) Ink injection of common bile duct in mouse samples. (*B*) TEM imaging of mouse samples. (*C*) Angiogenesis array with cholangiocyte supernatants from mouse models. (*D*) *Angpt1* and *Angpt2* mRNA expression in total liver samples from mouse models. (*E*) IPA linking ET-A with Angpt1 and Angpt2. Data are mean ± standard deviation. n = 5 mice per group analyzed for TEM; n = 3 reactions per group in cholangiocyte supernatant pooled from n = 8 mice per group; n = 9 reactions per group in RNA isolated from total liver from n = 6 mice per group. TEM is 2500× and 12,500×, scale bar = 2 μm. *$P < .05$, **$P < .01$, ***$P < .001$, ****$P < .0001$.

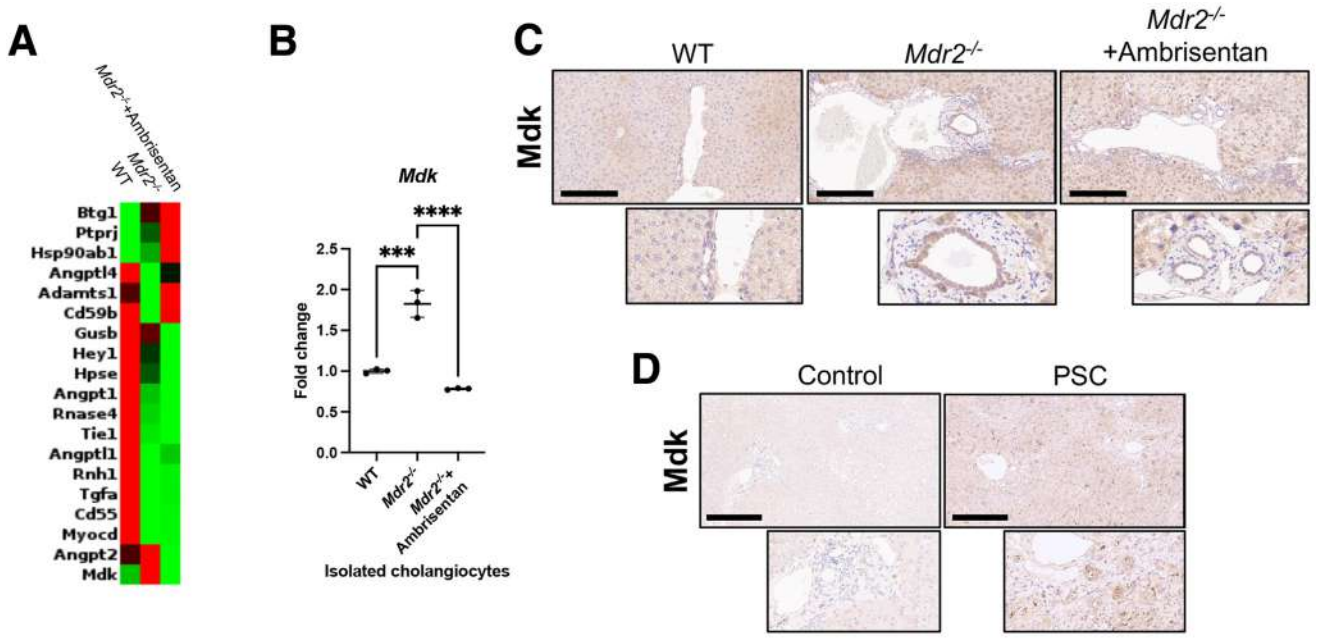

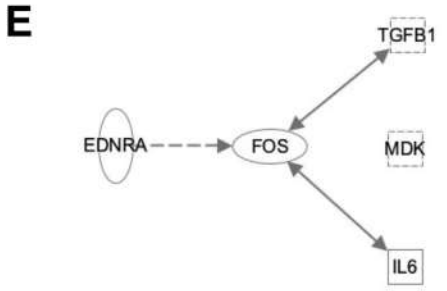

Start	End	Dissimilarity	String	RE equally	RE query
17	24	12.345273	CTGACCTC	0.01863	0.0164

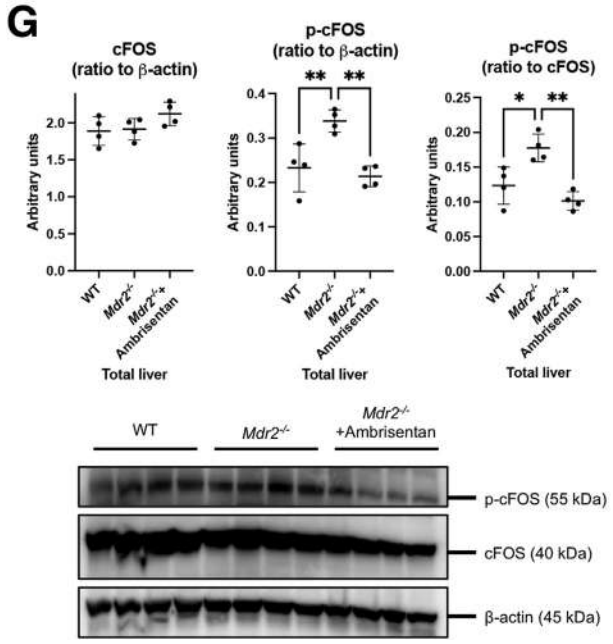

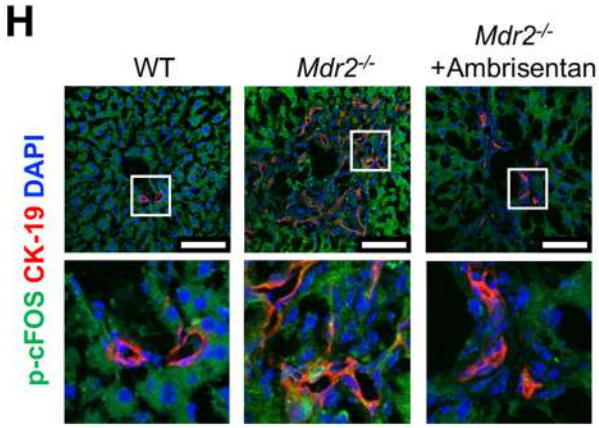

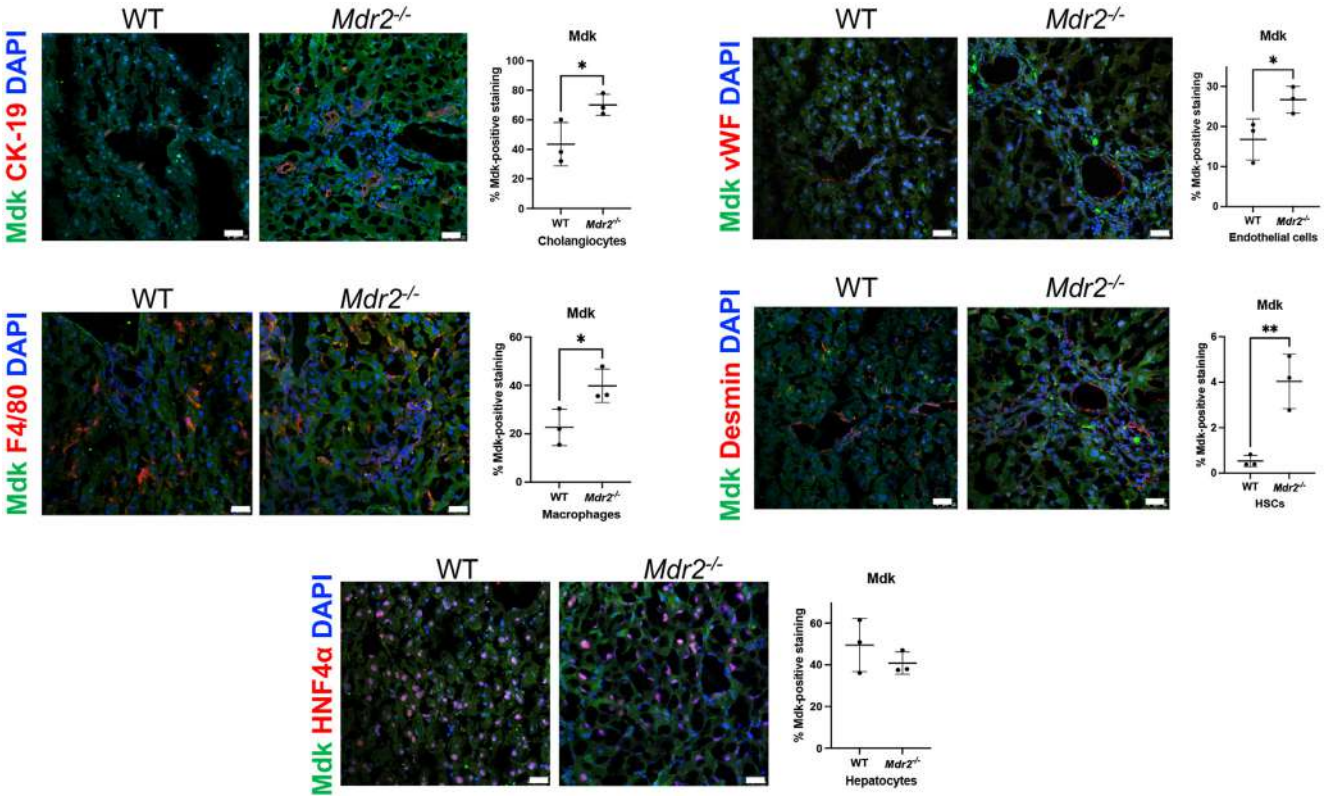

Figure 12. Mdk expression in different cells. Co-staining for Mdk and CK-19, vWF, F4/80, desmin, and HNF4α in mouse models. Co-stains are 80×, scale bar = 25 μm. *$P < .05$, **$P < .01$, ***$P < .001$, ****$P < .0001$.

cholangiocytes. Bead bound intrahepatic cholangiocytes were pulled down with a magnet and washed 3× with 1× HEPES-buffered saline, and number and viability were determined with trypan blue exclusion. For supernatant collection, 1×10^6 cholangiocytes/mL were incubated in 1× HEPES-buffered saline containing 0.01% (wt/vol) $MgSO_4$ and 3.4 mmol/L $CaCl_2$ for 4 hours in a 37°C shaking water bath before collecting supernatants.

Human Samples and Cholangiocyte Isolation

Serum, bile, and liver (FFPE- and OCT-embedded) were obtained from PSC patients with end-stage liver disease and non-diseased controls as explant from liver transplant or deceased donors, respectively, by Dr Burcin Ekser under a protocol approved by the Indiana University School of Medicine. The protocol was reviewed and approved by the Veterans' Administration IRB and R&D committees and by the Indiana University School of Medicine IRB committee. Additional human non-diseased control liver samples (FFPE- and OCT-embedded) were purchased from Sekisui XenoTech LLC (Kansas City, KS). All human research was conducted in accordance with both the Declarations of Helsinki and Istanbul. Demographics of the human samples are detailed in Table 3. Serum, bile, and liver samples were not matched and were obtained from separate sets of patients.

IH and EH cholangiocytes isolated from donors (3 control and 3 late-stage PSC) were obtained 3–8 hours after cross-clamp and in situ perfusion and were preserved in histidine-tryptophan-ketoglutarate solution at 4°C until further processing. We used both IH and EH cholangiocytes because of the difficult isolation process for IH cholangiocytes and the low number of isolated cells available for analysis. IH cholangiocytes (n = 1 control, n = 2 late-stage PSC) were isolated as follows.[72] Donor livers were obtained 3–8 hours after cross-clamp and in situ perfusion and were preserved in histidine-tryptophan-ketoglutarate solution at 4°C until further processing. A wedge-cut liver explant from the right lobe or the whole left lobe

Figure 11. (***See previous page***). **Mdk expression after Ambrisentan treatment.** (*A*) PCR array for angiogenic growth factors in isolated cholangiocytes from mouse models. (*B*) *q*PCR for *Mdk* in isolated cholangiocytes from mouse models. Staining for Mdk in (*C*) mouse models and (*D*) human samples. (*E*) IPA for ET-A with TGF-β1, MDK, and IL-6. (*F*) PROMO predictive binding for cFOS on the *MDK* promoter region. (*G*) Western blotting for cFOS, p-cFOS, and β-actin in mouse samples. (*H*) p-cFOS/CK-19 co-staining in mouse models. Data are mean ± standard deviation. n = 3 reactions in total RNA isolated from cholangiocytes isolated from n = 8 mice per group for PCR array and *q*PCR; n = 1 band per mouse from n = 4 mice per group for Western blotting. Mdk immunohistochemistry is 20× and 40×, scale bar = 200 μm. p-cFOS/CK-19 co-stain is 40× and 120×, scale bar = 75 μm. *$P < .05$, **$P < .01$, ***$P < .001$, ****$P < .0001$.

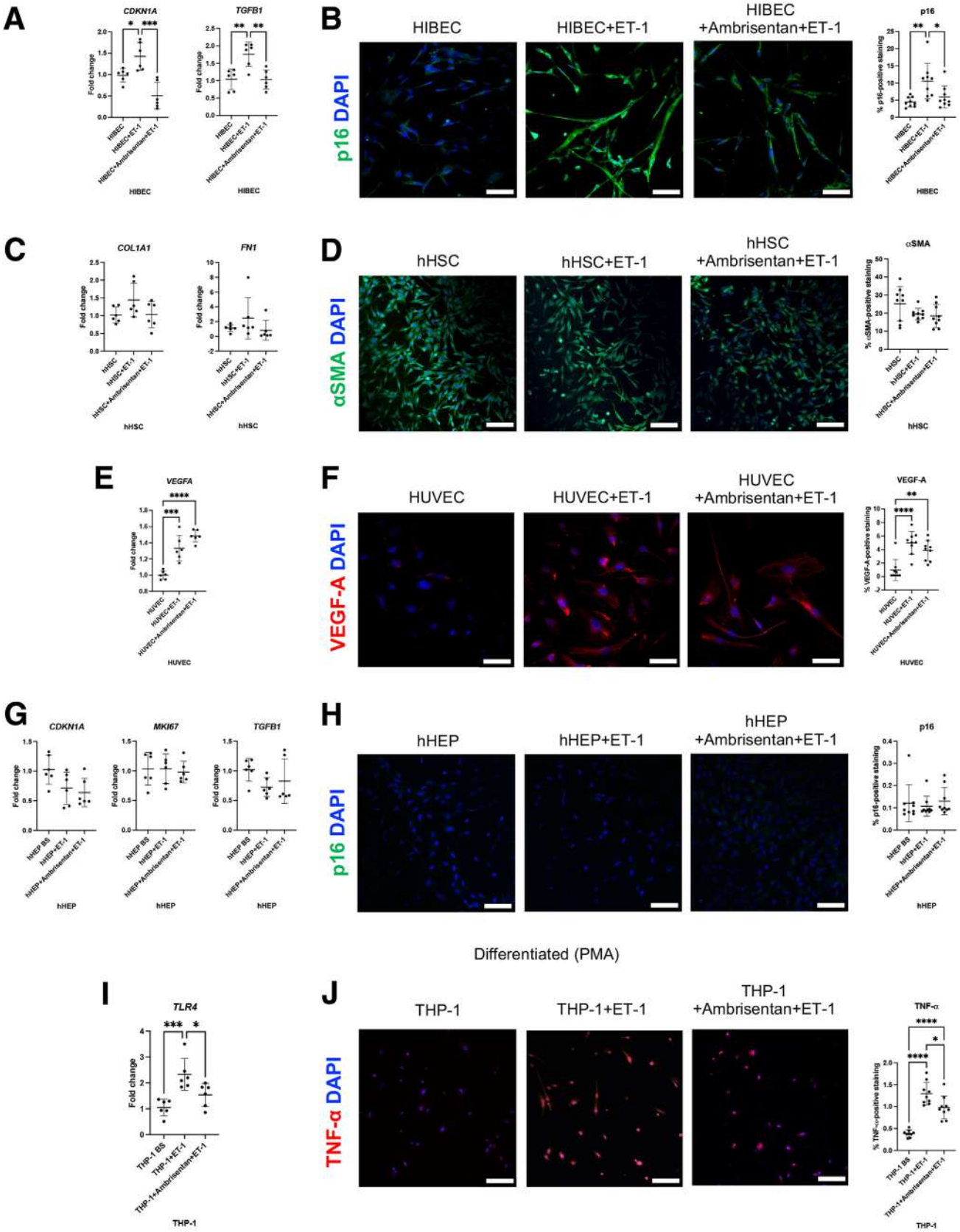
A
CDKN1A
TGFB1
Fold change
HIBEC
HIBEC+ET-1
HIBEC+Ambrisentan+ET-1
B
HIBEC
HIBEC+ET-1
HIBEC +Ambrisentan+ET-1
p16 DAPI
p16
% p16-positive staining
C
COL1A1
FN1
hHSC
hHSC+ET-1
hHSC+Ambrisentan+ET-1
D
hHSC
hHSC+ET-1
hHSC +Ambrisentan+ET-1
αSMA DAPI
αSMA
% αSMA-positive staining
E
VEGFA
HUVEC
HUVEC+ET-1
HUVEC+Ambrisentan+ET-1
F
HUVEC
HUVEC+ET-1
HUVEC +Ambrisentan+ET-1
VEGF-A DAPI
VEGF-A
% VEGF-A-positive staining
G
CDKN1A
MKI67
TGFB1
hHEP BS
hHEP+ET-1
hHEP+Ambrisentan+ET-1
hHEP
H
hHEP
hHEP+ET-1
hHEP +Ambrisentan+ET-1
p16 DAPI
p16
% p16-positive staining
Differentiated (PMA)
I
TLR4
THP-1 BS
THP-1+ET-1
THP-1+Ambrisentan+ET-1
THP-1
J
THP-1
THP-1+ET-1
THP-1 +Ambrisentan+ET-1
TNF-α DAPI
TNF-α
% TNF-α-positive staining

was used for cell isolation, and the Glisson's capsule was preserved. Cholangiocytes from human control (n = 1) and late-stage PSC (n = 2) were obtained using sterile techniques. Fresh liver tissue was manually dissociated with scissors and rinsed 3 times with 1× phosphate-buffered saline. Next, liver pieces were digested in 1.66 mg/mL collagenase type XI (Sigma-Aldrich) diluted in Dulbecco modified Eagle medium-F12 (Lonza, Walkersville, MD) containing 10% antibiotic-antimycotic in a 37°C shaking water bath for 30 minutes. The digested liver tissue was filtered through gauze, and the resulting lysate was filtered again with a 100-μm cell strainer. The resulting lysate was centrifuged at 100*g* for 4 minutes at 4°C, and the pellet was discarded. The supernatant was collected and again centrifuged at 700*g* for 5 minutes; the supernatant was discarded, and the pellet (containing non-parenchymal cells) was washed in DMEM-F12 containing 10% antibiotic-antimycotic. This cell suspension was centrifuged at 700*g* for 5 minutes at 4°C; the resulting supernatant was discarded, and the pellet was resuspended in H69 medium and placed into collagen-coated cellware. The non-parenchymal cell fraction was grown until confluency, at which time the cells were trypsinized and cholangiocytes purified using EpCAM (HEA125; Progen, Wayne, PA) tagging and selection by fluorescence activated cell sorting. EH cholangiocytes were isolated from donor control (n = 2) and late-stage PSC (n = 1) common bile ducts, which were preserved in histidine-tryptophan-ketoglutarate solution at 4°C until further processing, by gentle scraping. Cells were grown on collagen-coated cellware until confluent and then trypsinized and cholangiocytes purified using EpCAM (HEA125; Progen) tagging and selection by fluorescence activated cell sorting. Primary human IH and EH cholangiocytes were immortalized by transduction with lentivirus expressing Human Papillomavirus Type 16 E6 and E7 oncoproteins (Applied Biological Materials Inc, Richmond, BC, Canada).

Expression and Secretion of ET-1, ET-2, and ET-A

ET-1, ET-2, and ET-A expression was analyzed by immunohistochemistry in mouse and human liver sections and by *q*PCR (gene names *EDN1*, *EDN2* and *EDNRA*) in human cholangiocytes. ET-1, ET-2, and ET-A expression was evaluated in cholangiocytes and endothelial cells by immunofluorescent co-stain with CK-19 and vWF, respectively. ET-1 and ET-2 levels were measured in isolated mouse cholangiocyte supernatants and in human bile and cholangiocyte supernatants using the Endothelin-1 Quantikine ELISA Kit (R&D Systems, Minneapolis, MN) and Endothelin-2 ELISA Kit (LSBio, Seattle, WA).

Histopathology, Ductular Reaction, and Biliary Senescence

H&E staining was performed in liver, lung, heart, and kidney sections, because these organs have high ET-A expression,[9] and used to evaluate histopathologic changes using H&E Stain Kit (Vector Laboratories, Burlingame, CA). H&E staining was scored in a blinded fashion.

Ductular reaction was evaluated in mouse models using immunohistochemistry for CK-19 and semiquantitative analysis using the Image-Pro Analyzer (Media Cybernetics, Rockville, MD). Macroscopic analysis of biliary network expansion was visualized by ink injection as described.[73] Ink is slowly injected directly into the common bile duct to allow for complete perfusion of the IH biliary tree[73]; this allows us to evaluate bile duct expansion and ductular reaction.

Biliary senescence was determined by immunofluorescence for p16 co-stained with CK-19 and senescence-associated β galactosidase (SA-β-Gal) activity using the Senescence β-Galactosidase Staining Kit (Cell Signaling Technology, Danvers, MA); images were quantified using the Image-Pro Analyzer. The senescent factor, TGF-β1, was imaged in bile ducts by co-staining with CK-19, as well as vWF (to relate with endothelial cells). In addition, mRNA levels of *Cdkn1a* and *Tgfb1* were measured by *q*PCR in isolated cholangiocytes.

Inflammation, Immune Cell Infiltration, and Liver Fibrosis

Macrophage infiltration was assessed by immunohistochemistry for F4/80, which was semiquantified using the Image-Pro Analyzer. T-cell ($CD3^+$) and B-cell ($CD20^+$) infiltration was visualized by immunohistochemistry. The numbers of $CD3^+$ and $CD20^+$ cells were counted in portal tracts and expressed as the number of cells per high-power field at 40× magnification. At least 10 different portal tracts were analyzed per group. The mRNA expression of C-C motif chemokine ligand 2 (*Ccl2*) and *Ccl5* was determined in total liver by *q*PCR.

Collagen deposition was determined by Sirius Red staining with Fast Green counterstain (Sirius Red/Fast Green) and Masson's trichrome staining. Sirius Red/Fast Green images were quantified using the Image-Pro Analyzer. *Col1a1* were measured by *q*PCR in total liver. We measured hydroxyproline levels in total liver (20 mg) using the Hydroxyproline Assay Kit (Sigma-Aldrich). HSC presence was visualized by immunofluorescence for desmin co-stained with CK-19, and desmin-positive staining was quantified using the Image-Pro Analyzer. The relationship between ductular reaction and liver fibrosis was assessed by

Figure 13. (***See previous page***). ***In vitro* cell response to ET-1/ET-A signaling.** (*A*) *q*PCR for *CDKN1A* and *TGFB1* and (*B*) p16 immunofluorescence in treated HIBECs. (*C*) *q*PCR for *COL1A1* and *FN1* and (*D*) αSMA immunofluorescence in treated hHSCs. (*E*) *q*PCR for *VEGFA* and (*F*) VEGF-A immunofluorescence in treated HUVECs. (*G*) *q*PCR for *CDKN1A*, *MKI67*, and *TGFB1* and (*H*) p16 immunofluorescence in treated hHEPs. (*I*) *q*PCR for *TLR4* and (*J*) tumor necrosis factor-α immunofluorescence in treated THP-1. Data are mean ± standard deviation. All treatments performed n = 3 times per group. n = 2 reactions per treatment for *q*PCR. n = 3 images analyzed per treatment for staining. Staining is 40×, scale bar = 100 μm. **P* < .05, ***P* < .01, ****P* < .001, *****P* < .0001.

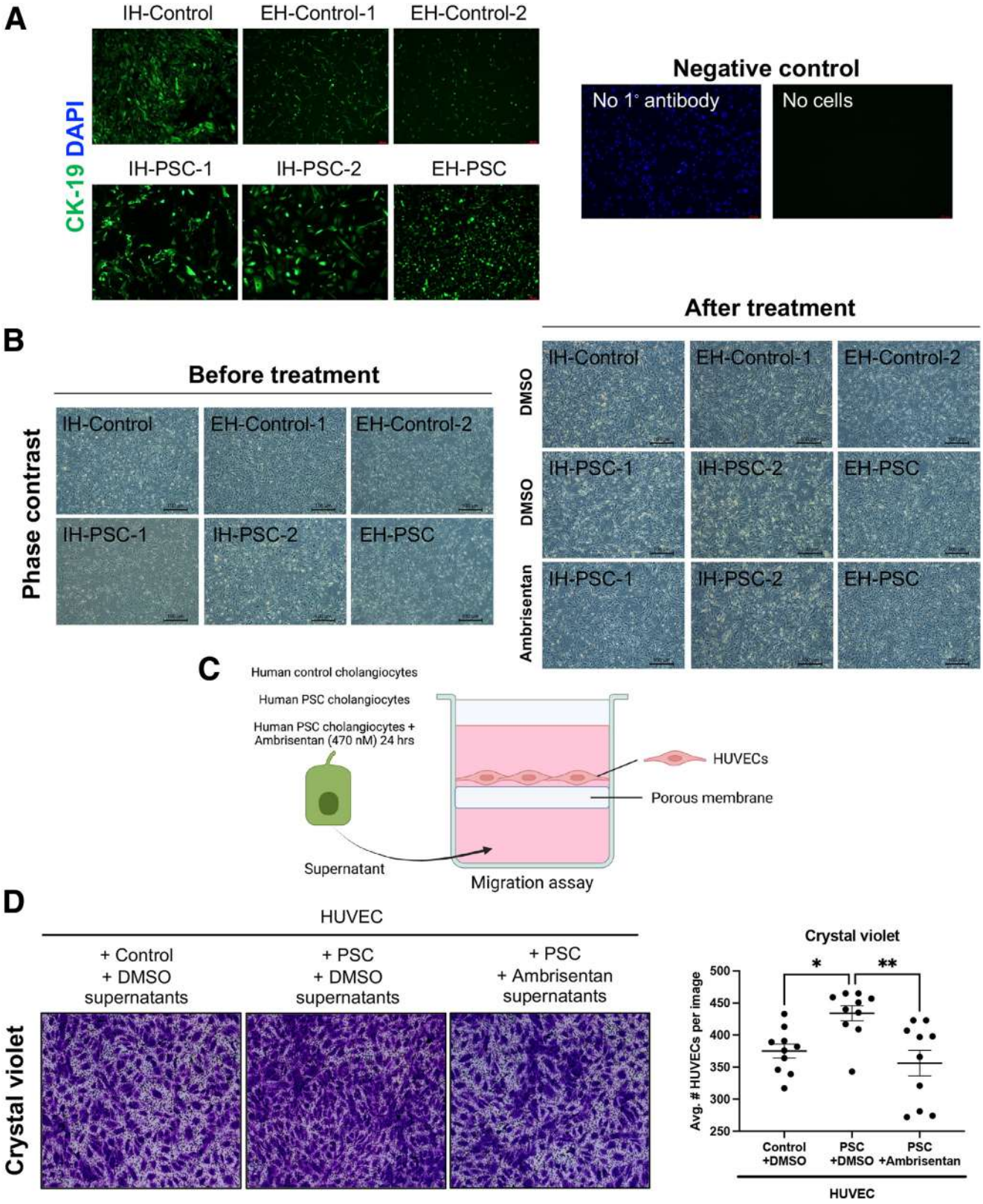

Figure 14. ***In vitro*** **HUVEC migration assay.** (*A*) CK-19 staining and negative controls in isolated control and PSC cholangiocytes. (*B*) Phase contrast microscopy for control and PSC cholangiocytes before and after treatment. (*C*) Illustration of migration assay setup. (*D*) Crystal violet staining and semiquantification of migration assay. Data are mean ± standard deviation. n = 2 wells per HUVEC treatment (supernatants pooled from n = 3 control and PSC cholangiocytes) and n = 5 images per well for migration assay. Illustration made with BioRender.com. Images are 20×. *$P < .05$, **$P < .01$, ***$P < .001$, ****$P < .0001$.

Table 1. List of Antibodies

Antibody	Use, dilution	Reactivity	Company	Catalog no.
α-Smooth muscle actin (α-SMA)	IF, 1:100	Human	Abcam	ab5694
β-Actin	WB, 1:2000	Mouse, Human	Santa Cruz	SC47778
cFOS	WB, 1:1000	Mouse	Abcam	ab214672
Cluster of differentiation 3 (CD3)	IHC, 1:100	Mouse	Abcam	ab5690
Cluster of differentiation 20 (CD20)	IHC, 1:100	Mouse	Abcam	ab64088
Cluster of differentiation 31 (CD31)	IHC, 1:50	Mouse, Human	Abcam	ab28364
Cytokeratin-19 (CK-19)	IHC, 1:200	Mouse	Abcam	ab52625
Cytokeratin-19 (CK-19)	IF, 1:200	Mouse, Human	Developmental Studies Hybridoma Bank	TROMA-III (Krt19)
Desmin	IF, 1:200	Mouse	Abcam	ab15200
Desmin	IF (Mdk co-stain) 1:20	Mouse	R&D Systems	AF-3844
Endothelin-1 (ET-1)	IF, 1:500 and IHC, 1:200	Mouse, Human	Abcam	ab117757
Endothelin-2 (ET-2)	IF, 1:100 and IHC, 1:100	Mouse, Human	MyBioSource	MBS2518418
Endothelin receptor-A (ET-A)	IF, 1:100 and IHC, 1:200	Mouse, Human	Abcam	ab30536
F4/80	IHC, 1:200	Mouse	Cell Signaling Technology	70076S
F4/80	IF, 1:100	Mouse	Invitrogen	14-4081-82
Hepatocyte nuclear factor (HNF)4α	IF, 1:100	Mouse	LS Bio	LS-C758303
Midkine (Mdk)	IHC, 1:100 and IF, 1:100	Mouse, Human	Invitrogen	PA5-115560
Phospho-cFOS (p-cFOS)	IF, 1:100	Mouse	Cell Signaling Technology	5348
Cyclin-dependent kinase inhibitor 2A (p16)	IF, 1:100 (mouse) and 1:50 (human)	Mouse, Human	Abcam	ab189034
Transforming growth factor-β1 (TGF-β1)	IF, 1:100	Mouse, Human	Abcam	ab92486
Tumor necrosis factor (TNF)-α	IF, 1:100	Human	Abcam	ab6671
Vascular endothelial growth factor-A (VEGF-A)	IF, 1:250 and IHC, 1:200	Mouse, Human	Abcam	ab52917
VEGF-A	WB, 1:1000	Mouse, Human	Abcam	ab214424
vonWillebrand factor (vWF)	IF, 1:200	Mouse	Abcam	ab8822

IF, immunofluorescence; IHC, immunohistochemistry; WB, Western blot.

immunohistochemistry for CK-19 co-stained with Sirius Red/Fast Green.

Liver Angiogenesis and Angiogenic Signaling

Angiogenesis was visualized by immunofluorescence for vWF co-stained with CK-19. The vWF staining was semi-quantified using the Image-Pro Analyzer. CD31 immunostaining was performed, and the number of $CD31^+$ vessels was counted in portal tracts and expressed as vessels per portal tract (at least 10 different portal tracts were analyzed for each mouse).

Pro-angiogenic VEGF-A was evaluated by immunohistochemistry. The percentage of VEGF-A–positive cholangiocytes was calculated by an algorithm (ImageScope), and then a semiquantitative score was applied (0, $\leq$1%; 1, 1%–10%; 2, 10%–30%; 3, 30%–50%; 4, $\geq$50%). The mRNA expression of *Vegfa* was determined in total liver by *q*PCR. Expression of VEGF-A was validated in protein from total liver (40 μg) by Western blotting; β-actin was used as the housekeeping protein. Vessel stabilizing angiopoietin (*Angpt*)1 and pro-angiogenic *Angpt2* were evaluated by *q*PCR in total liver samples. TGF-β1 localization in endothelial cells (pro-angiogenic) was evaluated by co-staining with vWF. TGF-β1 secretion was measured in mouse cholangiocyte supernatants using the TGF-β1 Quantikine ELISA (R&D Systems). IPA determined a link between ET and TGF-β1, Angpt1 and Angpt2. Cholangiocyte secretion of angiogenic factors was determined in isolated cholangiocyte supernatants using the Mouse Angiogenesis ELISA (Signosis, Santa Clara, CA).

Angiogenic factor expression was evaluated in isolated cholangiocytes using the Mouse Angiogenic Growth Factors RT^2 Profiler PCR Array (Qiagen, Valencia, CA). Changes in *Mdk* were validated by *q*PCR in isolated cholangiocytes to verify the trend. IPA determined the link between ET-A and

Table 2. List of Primers Used

Primer	Species	Company	GeneGlobe ID
β-actin (*Actb*)	Mouse	Qiagen	PPM02945B-200
Angiopoietin-1 (*Angpt1*)	Mouse	Qiagen	PPM03054F-200
Angiopoietin-2 (*Angpt2*)	Mouse	Qiagen	PPM03729F-200
C-C motif ligand 2 (*Ccl2*)	Mouse	Qiagen	PPM03151G-200
C-C motif ligand 5 (*Ccl5*)	Mouse	Qiagen	PPM02960F-200
Cyclin-dependent kinase 1a (*Cdkn1a*)	Mouse	Qiagen	PPM02901B-200
Collagen, type 1, α1 (*Col1a1*)	Mouse	Qiagen	PPM03845F-200
Midkine (*Mdk*)	Mouse	Qiagen	PPM03800D-200
Ribosomal protein s18 (*Rps18*)	Mouse	Qiagen	PPM28991A-200
Transforming growth factor-β1 (*Tgfb1*)	Mouse	Qiagen	PPM02991B-200
Vascular endothelial growth factor-a (*Vegfa*)	Mouse	Qiagen	PPM03041F-200
β-actin (*ACTB*)	Human	Qiagen	PPH00073G-200
CDKN1A	Human	Qiagen	PPH00211E-200
COL1A1	Human	Qiagen	PPH01299F-200
Endothelin-1 (*EDN1*)	Human	Qiagen	PPH00653A-200
Endothelin-2 (*EDN2*)	Human	Qiagen	PPH02568C-200
Endothelin receptor-A (*EDNRA*)	Human	Qiagen	PPH00669B-200
Fibronectin 1 (*FN1*)	Human	Qiagen	PPH00143B-200
Marker of proliferation Ki67 (*MKI67*)	Human	Qiagen	PPH01024E-200
Transforming growth factor-β1 (*TGFB1*)	Human	Qiagen	PPH00508A-200
Toll-like receptor 4 (*TLR4*)	Human	Qiagen	PPH01024E-200
RPS18	Human	Qiagen	PPH60076B-200
VEGFA	Human	Qiagen	PPH00251C-200

Mdk. Hepatic Mdk immunoreactivity in mouse models and human samples was evaluated by immunohistochemistry. Cellular expression of Mdk was evaluated in mouse models by immunofluorescent co-staining with CK-19 (cholangiocytes), vWF (portal vascular endothelial cells), F4/80 (macrophages), desmin (HSCs), and HNF4α (hepatocytes); Mdk expression in each cell type was quantified using Image-Pro Analyzer.

TEM

Liver tissues ($\sim$2 mm^3) were fixed in 2% paraformaldehyde, 2.5% glutaraldehyde, and 100 mmol/L cacodylate buffer (Electron Microscopy Sciences, Hatfield, PA) for 2 hours at room temperature and then overnight at 4°C. Samples were washed in sodium cacodylate buffer at room temperature and post-fixed in 2% osmium tetroxide (Ted Pella Inc, Redding, CA) for 1 hour at room temperature. Samples were rinsed in dH_2O, dehydrated in a graded series of ethanol, and embedded in Eponate 12 resin (Ted Pella Inc). Sections of 95 nm were cut with a Leica Ultracut UCT ultramicrotome (Leica Microsystems Inc, Bannockburn, IL), stained with uranyl acetate and lead citrate, and viewed on a JEOL 1200 EX transmission electron microscope (JEOL USA Inc, Peabody, MA) equipped with an AMT 8-megapixel digital camera and AMT Image Capture Engine V602 software (Advanced Microscopy Techniques, Woburn, MA).

Downstream Signaling

IPA was used to evaluate a mechanistic link between ET-A and IL-6, TGF-β1, and Mdk. Specifically, in Path Explorer we looked for direct mechanisms that were downstream of ET-A (human and mouse species). No miRNA links were suggested, and when parsing through the transcription factors, the only one that had multiple links was FOS (ie, cFOS). Levels of total cFOS and p-cFOS were determined in protein from total liver (40 μg) by Western blotting; β-actin was used as the housekeeping protein. Changes in p-cFOS in bile ducts were determined by immunostaining. To predict cFOS binding to our gene of interest, *MDK*, we used PROMO version 3.0.2.[74,75] Specifically, in PROMO we selected human factors and sites and selected c-FOS (T00123) as the factor of interest. The promoter region of the *MDK* gene (from −100 bp to 10 bp) was parsed for potential binding sites. The dissimilarity threshold, which determines how similar a sequence is to the known binding site, was set to 15%. PROMO calculated the random expectation (RE) that determines the number of matches to occur in a random sequence; RE equally evaluates the equiprobability for the 4 nucleotides, and RE query estimates the nucleotide probability as the nucleotide frequencies in the sequence.

In Vitro *Effects of Ambrisentan on Various Hepatic Cells*

We wanted to evaluate the cell-specific effect of ET-1/ET-A signaling on different liver cells. To address this, we

Table 3. Patient Demographics and Samples Used

Diagnosis	Sample type	Source	Sex	Age (y)
Control	Bile	IU	Female	54
Control	Bile	IU	Female	34
Control	Bile	IU	Female	23
Control	Bile	IU	Female	62
Control	Bile	IU	Female	59
Control	Bile	IU	Male	38
Control	Bile	IU	Male	42
Control	Bile	IU	Male	39
Control	Isolated cholangiocytes (IH-Control)	IU	Male	1.3
Control	Isolated cholangiocytes (EH-Control-1)	IU	Male	24
Control	Isolated cholangiocytes (EH-Control-2)	IU	Male	29
Control	Liver sections	IU	Normal	46
Control	Liver sections	IU	Male	50
Control	Liver sections	IU	Male	25
Control	Liver sections	Xenotech	Female	56
Control	Snap-frozen liver	Xenotech	Female	17
Control	Snap-frozen liver	Xenotech	Female	24
Control	Snap-frozen liver	Xenotech	Male	55
Control	Snap-frozen liver	Xenotech	Female	31
Control	Liver sections, snap-frozen liver	Xenotech	Female	58
Control	Liver sections, snap-frozen liver	Xenotech	Female	52
Control	Liver sections, snap-frozen liver	Xenotech	Male	46
Control	Liver sections, snap-frozen liver	Xenotech	Female	62
PSC (end-stage)	Snap-frozen liver	IU	Male	55
PSC (end-stage)	Snap-frozen liver	IU	Male	60
PSC (end-stage)	Snap-frozen liver	IU	Male	61
PSC (end-stage)	Snap-frozen liver	IU	Male	33
PSC	Isolated cholangiocytes (IH-PSC-1)	IU	Female	56
PSC	Isolated cholangiocytes (IH-PSC-2)	IU	Male	60
PSC	Isolated cholangiocytes (EH-PSC)	IU	Male	55
PSC (end-stage)	Bile, liver sections	IU	Male	38
PSC (Crohn's disease)	Bile, liver sections	IU	Female	46
PSC (ulcerative colitis)	Bile, liver sections	IU	Female	46
PSC (end-stage)	Bile, snap-frozen liver	IU	Female	56
PSC (end-stage)	Liver sections, snap-frozen liver	IU	Female	45
PSC (not cirrhotic)	Bile, liver sections, snap-frozen liver	IU	Male	32

IU, Indiana University; PSC, primary sclerosing cholangitis.

treated human HIBECs, hHSC (also known as HHSteC; ScienCell, Carlsbad, CA), HUVECs (Lonza; Basel, Switzerland), human hepatocytes (hHEP) (ScienCell), and human macrophages (differentiated from THP-1 cells, TIB-202; ATCC, Manassas, VA) with Ambrisentan (470 nmol/L) for 24 hours before treatment with ET-1 (100 nmol/L) for 24 hours, basal (DMSO) for 24 hours, or ET-1 (100 nmol/L) for 24 hours. Before treatments, THP-1 cells (provided as circulating monocytes) were stimulated with phorbol 12-myristate 13-acetate (PMA, 200 nmol/L; Sigma-Aldrich) for 48 hours to allow for full differentiation to macrophages. To understand if ET-1 induced cellular changes via ET-A, we measured (1) *CDKN1A* and *TGFB1* by *q*PCR and p16 by immunostaining in treated HIBECs; (2) *COL1A1* and *FN1* by *q*PCR and αSMA by immunostaining in treated hHSCs; (3) *VEGFA* by *q*PCR and VEGF-A by immunostaining in treated HUVECs; (4) *CDKN1A*, *MKI67,* and *TGFB1* by *q*PCR and p16 by immunostaining in treated hHEPs; and (5) *TLR4* by *q*PCR and tumor necrosis factor-α by immunostaining in differentiated and treated THP-1 cells. All immunofluorescent stains were quantified by ImageJ (NIH).

In Vitro *HUVEC Migration Assay*

Human PSC cholangiocytes were treated with Ambrisentan (470 nmol/L) or vehicle (DMSO) for 24 hours, and human control cells were treated with a vehicle to ensure changes in PSC cells were not due to DMSO-induced damage. HUVECs were plated in the top chamber of the migration Transwell (3 μM pore size; Corning Inc, Tewksbury, MA), and the cells were serum starved for 12 hours before stimulation with 50 μL supernatants (pooled from all treated control or PSC cholangiocytes) placed in the lower chamber. After 12 hours, cell migration was evaluated by 0.1% crystal violet staining of the membrane, and the number of migrated HUVECs was manually counted.

Statistical Analysis

All authors had access to the study data and had reviewed and approved the final manuscript. Data are expressed as dot plots showing mean $\pm$ standard deviation. Differences were analyzed by Student unpaired t test (two-tailed) when 2 groups were analyzed and by one-way analysis of variance (two-tailed) when more than 2 groups were analyzed. Two-way analysis of variance (two-tailed) was used to analyze the angiogenesis array. Tukey's multiple comparison's post hoc test was used with one-way and two-way analysis of variance. Pearson correlation coefficients (two-tailed) were used for correlative studies. $P < .05$ was considered significant. Statistical analyses were performed with GraphPad Prism (version 9.2.0; GraphPad Software, LLC, San Diego, CA).

References

1. Lazaridis KN, LaRusso NF. Primary sclerosing cholangitis. N Engl J Med 2016;375:1161–1170.
2. Sato K, Marzioni M, Meng F, et al. Ductular reaction in liver diseases: pathological mechanisms and translational significances. Hepatology 2019;69:420–430.
3. Konigshofer P, Hofer BS, Brusilovskaya K, et al. Distinct structural and dynamic components of portal hypertension in different animal models and human liver disease etiologies. Hepatology 2022;75:610–622.
4. Coll M, Arino S, Martinez-Sanchez C, et al. Ductular reaction promotes intrahepatic angiogenesis through Slit2-Roundabout 1 signaling. Hepatology 2022;75:353–368.
5. de Jong IEM, Overi D, Carpino G, et al. Persistent biliary hypoxia and lack of regeneration are key mechanisms in the pathogenesis of posttransplant nonanastomotic strictures. Hepatology 2022;75:814–830.
6. Kyritsi K, Kennedy L, Meadows V, et al. Mast cells induce ductular reaction mimicking liver injury in mice through mast cell-derived transforming growth factor beta 1 signaling. Hepatology 2021;73:2397–2410.
7. Kennedy L, Meadows V, Kyritsi K, et al. Amelioration of large bile duct damage by histamine-2 receptor vivo-morpholino treatment. Am J Pathol 2020;190:1018–1029.
8. Tsuneyama K, Ohba K, Zen Y, et al. A comparative histological and morphometric study of vascular changes in idiopathic portal hypertension and alcoholic fibrosis/cirrhosis. Histopathology 2003;43:55–61.
9. Davenport AP, Hyndman KA, Dhaun N, et al. Endothelin. Pharmacol Rev 2016;68:357–418.
10. Schneider MP, Boesen EI, Pollock DM. Contrasting actions of endothelin ET(A) and ET(B) receptors in cardiovascular disease. Annu Rev Pharmacol Toxicol 2007;47:731–759.
11. Cho JJ, Hocher B, Herbst H, et al. An oral endothelin-A receptor antagonist blocks collagen synthesis and deposition in advanced rat liver fibrosis. Gastroenterology 2000;118:1169–1178.
12. Ling L, Kuc RE, Maguire JJ, et al. Comparison of endothelin receptors in normal versus cirrhotic human liver and in the liver from endothelial cell-specific ETB knockout mice. Life Sci 2012;91:716–722.
13. Bluhm RE, Frazer MG, Vore M, et al. Endothelins 1 and 3: potent cholestatic agents secreted and excreted by the liver that interact with cyclosporine. Hepatology 1993;18:961–968.
14. Isales CM, Nathanson MH, Bruck R. Endothelin-1 induces cholestasis which is mediated by an increase in portal pressure. Biochem Biophys Res Commun 1993;191:1244–1251.
15. Fickert P, Zollner G, Fuchsbichler A, et al. Ursodeoxycholic acid aggravates bile infarcts in bile duct-ligated and Mdr2 knockout mice via disruption of cholangioles. Gastroenterology 2002;123:1238–1251.
16. Ehling J, Bartneck M, Wei X, et al. CCL2-dependent infiltrating macrophages promote angiogenesis in progressive liver fibrosis. Gut 2014;63:1960–1971.
17. Corpechot C, Barbu V, Wendum D, et al. Hypoxia-induced VEGF and collagen I expressions are associated with angiogenesis and fibrogenesis in experimental cirrhosis. Hepatology 2002;35:1010–1021.
18. Reimegard J, Tarbier M, Danielsson M, et al. A combined approach for single-cell mRNA and intracellular protein expression analysis. Commun Biol 2021;4:624.
19. Tugues S, Fernandez-Varo G, Munoz-Luque J, et al. Antiangiogenic treatment with sunitinib ameliorates inflammatory infiltrate, fibrosis, and portal pressure in cirrhotic rats. Hepatology 2007;46:1919–1926.
20. DiSalvo J, Bayne ML, Conn G, et al. Purification and characterization of a naturally occurring vascular endothelial growth factor.placenta growth factor heterodimer. J Biol Chem 1995;270:7717–7723.
21. Zachary I. VEGF signalling: integration and multi-tasking in endothelial cell biology. Biochem Soc Trans 2003;31:1171–1177.
22. Chen CC, Manning AM. TGF-beta 1, IL-10 and IL-4 differentially modulate the cytokine-induced expression of IL-6 and IL-8 in human endothelial cells. Cytokine 1996;8:58–65.
23. Luo B, Tang L, Wang Z, et al. Cholangiocyte endothelin 1 and transforming growth factor beta1 production in rat experimental hepatopulmonary syndrome. Gastroenterology 2005;129:682–695.
24. Lambers C, Roth M, Zhong J, et al. The interaction of endothelin-1 and TGF-beta1 mediates vascular cell remodeling. PLoS One 2013;8:e73399.

25. Browatzki M, Schmidt J, Kubler W, et al. Endothelin-1 induces interleukin-6 release via activation of the transcription factor NF-kappaB in human vascular smooth muscle cells. Basic Res Cardiol 2000;95:98–105.
26. Tanos T, Marinissen MJ, Leskow FC, et al. Phosphorylation of c-Fos by members of the p38 MAPK family: role in the AP-1 response to UV light. J Biol Chem 2005;280:18842–18852.
27. Verstegen MMA, Roos FJM, Burka K, et al. Human extrahepatic and intrahepatic cholangiocyte organoids show region-specific differentiation potential and model cystic fibrosis-related bile duct disease. Sci Rep 2020;10:21900.
28. Koch DG, Bogatkevich G, Ramshesh V, et al. Elevated levels of endothelin-1 in hepatic venous blood are associated with intrapulmonary vasodilatation in humans. Dig Dis Sci 2012;57:516–523.
29. Saida K, Hashimoto M, Mitsui Y, et al. The prepro vasoactive intestinal contractor (VIC)/endothelin-2 gene (EDN2): structure, evolution, production, and embryonic expression. Genomics 2000;64:51–61.
30. Bloch KD, Hong CC, Eddy RL, et al. cDNA cloning and chromosomal assignment of the endothelin 2 gene: vasoactive intestinal contractor peptide is rat endothelin 2. Genomics 1991;10:236–242.
31. Iwashima A, Kobayashi M, Saida K, et al. Contraction and intracellular calcium-ion elevation of cultured human aortic smooth muscle cells by endothelin-1, vasoactive intestinal contractor (VIC) and the derivatives. In Vitro Cell Dev Biol Anim 1997;33:751–756.
32. McCartney SA, Ballinger AB, Vojnovic I, et al. Endothelin in human inflammatory bowel disease: comparison to rat trinitrobenzenesulphonic acid-induced colitis. Life Sci 2002;71:1893–1904.
33. Storey JD, Madeoy J, Strout JL, et al. Gene-expression variation within and among human populations. Am J Hum Genet 2007;80:502–509.
34. Vohra BP, Planer W, Armon J, et al. Reduced endothelin converting enzyme-1 and endothelin-3 mRNA in the developing bowel of male mice may increase expressivity and penetrance of Hirschsprung disease-like distal intestinal aganglionosis. Dev Dyn 2007;236:106–117.
35. Gandhi CR, Stephenson K, Olson MS. Endothelin, a potent peptide agonist in the liver. J Biol Chem 1990;265:17432–17435.
36. Tieche S, De Gottardi A, Kappeler A, et al. Overexpression of endothelin-1 in bile duct ligated rats: correlation with activation of hepatic stellate cells and portal pressure. J Hepatol 2001;34:38–45.
37. De Gottardi A, Biecker E, Koshy A, et al. Sensitivity to endothelin-1 is decreased in isolated livers of endothelial constitutive nitric oxide synthase knockout mice. Comp Hepatol 2006;5:9.
38. Zipprich A, Gittinger F, Winkler M, et al. Effect of ET-A blockade on portal pressure and hepatic arterial perfusion in patients with cirrhosis: a proof of concept study. Liver Int 2021;41:554–561.
39. Ikenaga N, Liu SB, Sverdlov DY, et al. A new Mdr2(-/-) mouse model of sclerosing cholangitis with rapid fibrosis progression, early-onset portal hypertension, and liver cancer. Am J Pathol 2015;185:325–334.
40. Gandhi CR, Kuddus RH, Uemura T, et al. Endothelin stimulates transforming growth factor-beta1 and collagen synthesis in stellate cells from control but not cirrhotic rat liver. Eur J Pharmacol 2000;406:311–318.
41. Gabriel A, Kuddus RH, Rao AS, et al. Down-regulation of endothelin receptors by transforming growth factor beta1 in hepatic stellate cells. J Hepatol 1999;30:440–450.
42. Reinehr R, Fischer R, Haussinger D. Regulation of endothelin-A receptor sensitivity by cyclic adenosine monophosphate in rat hepatic stellate cells. Hepatology 2002;36:861–873.
43. McKenna S, Gossling M, Bugarini A, et al. Endotoxemia induces IkappaBbeta/NF-kappaB-dependent endothelin-1 expression in hepatic macrophages. J Immunol 2015;195:3866–3879.
44. Elisa T, Antonio P, Giuseppe P, et al. Endothelin receptors expressed by immune cells are involved in modulation of inflammation and in fibrosis: relevance to the pathogenesis of systemic sclerosis. J Immunol Res 2015;2015:147616.
45. Govaere O, Cockell S, Van Haele M, et al. High-throughput sequencing identifies aetiology-dependent differences in ductular reaction in human chronic liver disease. J Pathol 2019;248:66–76.
46. Lemoinne S, Cadoret A, Rautou PE, et al. Portal myofibroblasts promote vascular remodeling underlying cirrhosis formation through the release of microparticles. Hepatology 2015;61:1041–1055.
47. Fickert P, Fuchsbichler A, Wagner M, et al. Regurgitation of bile acids from leaky bile ducts causes sclerosing cholangitis in Mdr2 (Abcb4) knockout mice. Gastroenterology 2004;127:261–274.
48. Koyama Y, Maebara Y, Hayashi M, et al. Endothelins reciprocally regulate VEGF-A and angiopoietin-1 production in cultured rat astrocytes: implications on astrocytic proliferation. Glia 2012;60:1954–1963.
49. Koda M, Bauer M, Krebs A, et al. Endothelin-1 enhances fibrogenic gene expression, but does not promote DNA synthesis or apoptosis in hepatic stellate cells. Comp Hepatol 2006;5:5.
50. Enholm B, Paavonen K, Ristimaki A, et al. Comparison of VEGF, VEGF-B, VEGF-C and Ang-1 mRNA regulation by serum, growth factors, oncoproteins and hypoxia. Oncogene 1997;14:2475–2483.
51. Sun L, Wang Y, Wang X, et al. PD-L1 promotes myofibroblastic activation of hepatic stellate cells by distinct mechanisms selective for TGF-beta receptor I versus II. Cell Rep 2022;38:110349.
52. Senavirathna LK, Huang C, Pushparaj S, et al. Hypoxia and transforming growth factor beta1 regulation of long non-coding RNA transcriptomes in human pulmonary fibroblasts. Physiol Rep 2020;8:e14343.
53. Oh H, Takagi H, Suzuma K, et al. Hypoxia and vascular endothelial growth factor selectively up-regulate angiopoietin-2 in bovine microvascular endothelial cells. J Biol Chem 1999;274:15732–15739.

54. Hegeman MA, Hennus MP, van Meurs M, et al. Angiopoietin-1 treatment reduces inflammation but does not prevent ventilator-induced lung injury. PLoS One 2010;5:e15653.
55. Korff T, Ernst E, Nobiling R, et al. Angiopoietin-1 mediates inhibition of hypertension-induced release of angiopoietin-2 from endothelial cells. Cardiovasc Res 2012;94:510–518.
56. Dinsmore C, Reiter JF. Endothelial primary cilia inhibit atherosclerosis. EMBO Rep 2016;17:156–166.
57. Tabibian JH, O'Hara SP, Splinter PL, et al. Cholangiocyte senescence by way of N-ras activation is a characteristic of primary sclerosing cholangitis. Hepatology 2014;59:2263–2275.
58. Gopinathan G, Milagre C, Pearce OM, et al. Interleukin-6 stimulates defective angiogenesis. Cancer Res 2015;75:3098–3107.
59. Weckbach LT, Groesser L, Borgolte J, et al. Midkine acts as proangiogenic cytokine in hypoxia-induced angiogenesis. Am J Physiol Heart Circ Physiol 2012;303:H429–H438.
60. Lautz T, Lasch M, Borgolte J, et al. Midkine controls arteriogenesis by regulating the bioavailability of vascular endothelial growth factor A and the expression of nitric oxide synthase 1 and 3. EBioMedicine 2018;27:237–246.
61. Salani D, Taraboletti G, Rosano L, et al. Endothelin-1 induces an angiogenic phenotype in cultured endothelial cells and stimulates neovascularization in vivo. Am J Pathol 2000;157:1703–1711.
62. Bahde R, Kapoor S, Viswanathan P, et al. Endothelin-1 receptor A blocker darusentan decreases hepatic changes and improves liver repopulation after cell transplantation in rats. Hepatology 2014;59:1107–1117.
63. Said EA, Al-Dughaishi S, Al-Hatmi W, et al. Human macrophages and monocyte-derived dendritic cells stimulate the proliferation of endothelial cells through midkine production. PLoS One 2022;17:e0267662.
64. Wu LC, Lu IW, Chung CF, et al. Antiproliferative mechanisms of quercetin in rat activated hepatic stellate cells. Food Funct 2011;2:204–212.
65. Mende S, Schulte S, Strack I, et al. Telmisartan plus propranolol improves liver fibrosis and bile duct proliferation in the PSC-like Abcb4-/- mouse model. Dig Dis Sci 2013;58:1271–1281.
66. Yi ET, Liu RX, Wen Y, et al. Telmisartan attenuates hepatic fibrosis in bile duct-ligated rats. Acta Pharmacol Sin 2012;33:1518–1524.
67. Hood JD, Cheresh DA. Role of integrins in cell invasion and migration. Nat Rev Cancer 2002;2:91–100.
68. Mahabeleshwar GH, Feng W, Phillips DR, et al. Integrin signaling is critical for pathological angiogenesis. J Exp Med 2006;203:2495–2507.
69. Patsenker E, Popov Y, Stickel F, et al. Pharmacological inhibition of integrin alphavbeta3 aggravates experimental liver fibrosis and suppresses hepatic angiogenesis. Hepatology 2009;50:1501–1511.
70. Caligiuri A, Glaser S, Rodgers RE, et al. Endothelin-1 inhibits secretin-stimulated ductal secretion by interacting with ETA receptors on large cholangiocytes. Am J Physiol 1998;275:G835–G846.
71. Bravo M, Raurell I, Barbera A, et al. Synergic effect of atorvastatin and ambrisentan on sinusoidal and hemodynamic alterations in a rat model of NASH. Dis Model Mech 2021:14.
72. Kennedy L, Carpino G, Owen T, et al. Secretin alleviates biliary and liver injury during late-stage primary biliary cholangitis via restoration of secretory processes. J Hepatol 2023;78:99–113.
73. Schaub JR, Huppert KA, Kurial SNT, et al. De novo formation of the biliary system by TGFbeta-mediated hepatocyte transdifferentiation. Nature 2018;557:247–251.
74. Messeguer X, Escudero R, Farre D, et al. PROMO: detection of known transcription regulatory elements using species-tailored searches. Bioinformatics 2002;18:333–334.
75. Farre D, Roset R, Huerta M, et al. Identification of patterns in biological sequences at the ALGGEN server: PROMO and MALGEN. Nucleic Acids Res 2003;31:3651–3653.

Received September 5, 2022. Accepted June 9, 2023.

Correspondence
Address correspondence to: Lindsey Kennedy, PhD, Department of Medicine, Indiana University School of Medicine, Department of Research, Richard L. Roudebush VA Medical Center, 702 Rotary Circle, Room 007, Indianapolis, Indiana 46202. e-mail: linkenn@iu.edu, Lindsey.Kennedy@va.gov.

Acknowledgments
The authors thank Dr Wandy Beatty (Washington University School of Medicine, St. Louis, MO) for assistance with the TEM protocol, imaging, and analysis, Dr Stacey Huppert (Cincinnati Children's Hospital Medical Center, Cincinnati, OH) for assisting with the ink injection studies, and Drs Tuan M. Tran and Jyoti Bhardwaj (Indiana University School of Medicine, Indianapolis, IN) for the THP-1 cells and PMA.

CRediT Authorship Contributions

Travis Owen (Investigation: Equal; Methodology: Equal; Validation: Equal; Writing – review & editing: Equal)

Guido Carpino (Software: Lead; Validation: Equal; Writing – review & editing: Equal)

Lixian Chen (Investigation: Supporting; Writing – review & editing: Equal)

Debjyoti Kundu (Investigation: Supporting; Writing – review & editing: Equal)

Payton Wills (Investigation: Supporting; Writing – review & editing: Equal)

Burcin Ekser (Resources: Equal; Writing – review & editing: Equal)

Paolo Onori (Resources: Equal; Writing – review & editing: Equal)

Eugenio Gaudio (Resources: Equal; Writing – review & editing: Equal)

Gianfranco Alpini (Funding acquisition: Equal; Resources: Equal; Writing – review & editing: Equal)

Heather Francis (Funding acquisition: Equal; Resources: Equal; Writing – review & editing: Equal)

Lindsey Kennedy (Conceptualization: Lead; Formal analysis: Lead; Funding acquisition: Lead; Investigation: Lead; Resources: Lead; Supervision: Lead; Visualization: Lead; Writing – original draft: Lead)

Conflicts of interest
The authors disclose no conflicts.

Funding
Supported by the John B. Hickam Endowed Chair, Gastroenterology and Hepatology, Medicine, Indiana University School of Medicine; the Indiana University Health-Indiana University School of Medicine Strategic Research Initiative; the Senior Career Scientist Award (IK6 BX004601), and the VA Merit award (5I01BX000574) to GA, the Career Scientist Award (IK6BX005226) and the VA Merit award (1I01BX003031) to HF, and Career Development Award-2 to LK (1IK2BX005306) from the United States Department of Veteran's Affairs, Biomedical Laboratory Research and Development Service; and NIH grants DK108959 and DK119421 (HF), DK054811, DK115184, DK076898, DK107310, DK110035, and DK062975 (GA). EG and PO were supported by Grants (Progetti di Ateneo) from Sapienza University of Rome, Rome, Italy. Portions of these studies were supported by resources at the Richard L. Roudebush VA Medical Center, Indianapolis, IN. The views expressed in this article are those of the authors and do not necessarily represent the views of the Department of Veterans Affairs.